Endogenous Osteocyte-Osteoclast Signaling Enables Bone Remodeling, Drug Response, and Cancer Invasion in a Nanoscale Calcified Bone-on-a-Chip Model

Mauricio G.C. Sousa[1,2,5] #, Avathamsa Athirasala[1,2,5] #, Daniela M. Roth[1,2,5], Mahshid Hosseini[1,2,5], Genevieve E. Romanowicz[7], Rebekka Duhen[1,2], May Anny A. Fraga[6], Sofia M. Vignolo[1,2,5], Aaron Doe[2], Jinho Lee[3], Jonathan V. Nguyen[5], Angela S.P. Lin[7], Cristiane M. Franca[1,2,5], Robert E. Guldberg[7], Luiz E. Bertassoni[1,2,3,4,5]

[1] Knight Cancer Precision Biofabrication Hub, Knight Cancer Institute, Oregon Health & Science University, Portland, Oregon, USA.

[2] Cancer Early Detection Advanced Research (CEDAR), Knight Cancer Institute, Oregon Health & Science University, Portland, Oregon, USA.

[3] Division of Oncological Sciences, Knight Cancer Institute, Oregon Health & Science University, Portland, Oregon, USA.

[4] Department of Biomedical Engineering, School of Medicine, Oregon Health & Science University, Portland, Oregon, USA.

[5] Department of Oral Rehabilitation and Biosciences, School of Dentistry, Oregon Health & Science University, Portland, Oregon, USA.

[6] Department of Restorative Dentistry, Faculdade de Odontologia de Piracicaba (FOP), Universidade Estadual de Campinas, Piracicaba, São Paulo, Brazil.

[7] Knight Campus for Accelerating Scientific Impact, University of Oregon, Eugene, Oregon, USA.

Corresponding author:

Luiz E. Bertassoni

Email: bertasso@ohsu.edu

# Equal contribution.

Abstract

Bone homeostasis depends on spatially orchestrated interactions among osteoclasts, osteoblasts, and osteocytes that are embedded within a unique extracellular matrix that is mineralized on the nanoscale. Reconstructing these interactions to enable autonomous cell differentiation and tissue remodeling has remained a significant challenge towards mimicking adequate bone physiology and disease in-vitro. Here, we present an engineered model that spatially defines the paracrine communication of heterogeneous cell populations within bone tissue that supports the rapid maturation of primary osteoblasts into osteocytes, the differentiation of immune cells into osteoclasts, and calcified tissue resorption within a mineralized cell-laden bone-like tissue. We demonstrate that nanoscale mineralization of cell-laden collagen hydrogels on-a-chip enhances osteoblast to osteocyte differentiation, whereas osteocytes in the matrix accelerate osteoclastogenesis and remodeling in a spatially defined manner without the need for exogenous growth factors. Osteocyte-dependent osteoclastogenesis on-a-chip outperformed conventional stimulation with RANKL and M-CSF, reproduced the clinical response of anti-resorptive drugs, and mimicked established tumor-bone interactions observed in invasive oral cancer. By replicating essential aspects of bone composition and function, this system provides a robust, self-regulated microphysiologic model to investigate bone remodeling, cancer-bone crosstalk, and therapeutic interventions.

Keywords: bone-on-a-chip, osteocytes, osteoclastogenesis, biomimetic bone

1. Main

Bone-related diseases, including fractures, cancers, and osteoporosis, imposed a global economic burden projected to exceed $25 billion in 2025 alone[1, 2, 3, 4]. Despite the growing demand for effective bone treatments, existing preclinical models fall short in capturing the complex and dynamic interplay between the cellular machinery and structural components of bone, thus considerably limiting our ability to unravel the mechanisms that govern bone homeostasis, remodeling, and disease[5, 6]. Bone is a dynamic organ system whose formation and homeostasis depend on a tightly orchestrated sequence of cell-cell and cell-matrix interactions occurring within a highly specialized microenvironment[7, 8, 9]. In its mature form, bone is composed of a densely mineralized collagen matrix that embeds cells in three dimensions (3D), forming a stiff, hierarchically organized tissue capable of sensing, adapting to, and remodeling in response to physiological demands.[10, 11, 12] This mineralization arises through a nanoscale process in which calcium and phosphate ions are precisely guided into collagen fibrils by matrix-regulating proteins, resulting in the formation of intrafibrillar hydroxyapatite crystals[13, 14, 15]. These nanoscale mineralized collagen fibrils define the architecture and mechanical stiffness of the matrix and, critically, establish the cell-binding and ionic domains that regulate cell behavior[16, 17, 18, 19, 20]. For example, it has been demonstrated that cells sense and respond to this mineralized environment through mechanotransductive and ion-mediated signaling pathways that are essential for osteoblast differentiation and osteocyte function[21, 22, 23]. Embedded in the matrix, osteocytes act as central regulators of bone remodeling. They secrete paracrine cues that modulate both osteoblast activity and the recruitment and differentiation of osteoclast precursors[24, 25]. Through this mechanism, osteocytes control the remodeling events that occur in bone tissue, including those involved in resorption, adaptation, and pathologic bone loss[26, 27, 28]. Engineering a human-relevant system that faithfully reproduces these dynamic and endogenously regulated cell-cell and cell-matrix interactions represents not only a complex challenge but a critical need.

Current in-vitro models fail to recapitulate many of the essential hallmarks of bone, including chemical, physical, and biological features[29]. Most rely on non-mineralized collagen matrices, or apatite-laden hydrogels that lack the biochemical complexity and mechanical cues of the native nanoscale-calcified bone matrix. Alternatives such as mineral-coated plates, bone

explants, and demineralized bone surfaces, though considered gold standards for studying bone resorption, replicate some of the properties of native bone while neglecting the complex interplay of cell-cell and cell-matrix communication that is known to result in a self-regulating remodeling unit that defines bone physiology[30, 31, 32]. For example, osteoclastogenesis in these models is typically induced through supraphysiologic supplementation with recombinant receptor activator of nuclear factor κB ligand (RANKL) and macrophage colony-stimulating factor (M-CSF), thereby bypassing the natural signaling hierarchy regulated by the communication between osteocytes, osteoblasts, and osteoclasts[33, 34]. Even advanced 3D and organ-on-a-chip platforms often feature osteoblasts on soft or non-calcified matrices and fail to recapitulate the spatial architecture of entrapped osteocytes in intrafibrillar mineralized collagen fibers or the paracrine loops that define the regulation of bone turnover[35, 36]. These limitations compromise the ability of current models to reproduce the temporal sequence of events that drive bone adaptation and resorption. Therefore, the relevance of existing engineered bone models to study drug response, pathophysiology, or cell-matrix interactions at the bone surface is limited. An autonomous microphysiological system that mimics established hallmarks of bone physiology - where a nanostructurally mineralized collagen matrix osteoblast to osteocyte differentiation, and osteocytes coordinate the activity of osteoclasts and osteoblasts - remains an unmet need in translational bone research.

To address these gaps, here we introduce a bone-on-a-chip platform that spatially organizes human osteoblasts, osteocytes, macrophages, osteoclasts, and endothelial cells within a nanostructured mineralized matrix, enabling the temporally-controlled cell state transitions that are essential for bone remodeling and self-regulation. Unlike conventional models, this microphysiological system supports terminal osteogenic differentiation (osteoblast to osteocyte) and functional osteoclastogenesis through endogenous cell-cell and cell-matrix communication without the need for exogenous supplements and growth factors. Moreover, this self-regulated system allows for osteoclast differentiation events via physiological pathways that are different from those observed with standard M-CSF- and RANKL-supplemented differentiation medium. The resulting system exhibits robust resorptive behavior observed via micro-CT, responds to clinical-grade anti-resorptive drugs, and mimics the invasion of oral squamous cell carcinoma (OSCC) into bone by recapitulating bone resorption in the progression of oral cancer. In summary, this biomimetic bone-on-a-chip platform addresses critical gaps in existing models by

authentically replicating the complex microenvironment of bone. This provides a novel and robust, physiologically relevant tool to study bone homeostasis, disease mechanisms, and therapeutic responses in-vitro for preclinical research in bone-targeting diseases and therapeutic interventions.

2. Results

2.1. Nanoscale matrix mineralization drives osteocyte differentiation and supports modular integration of vasculature

Bone is a hierarchical structure organized at the nanoscale level by mineralized collagen fibers, which are critical for osteocyte differentiation and the regulation of osteoclastogenic factors[37]. To replicate this nanostructure in vitro, we developed a biomimetic model by embedding osteoblasts in a collagen matrix (2.5 mg/mL) within a microfluidic device featuring a central channel flanked by two lateral channels that can be perfused independently (**Figure 1a**). The osteoblast-laden collagen matrix was injected into the main channel and underwent mineralization over a 3-day period. We followed a previously developed strategy to achieve mineralization using previously optimized media containing physiological levels of calcium (Ca^{2+}), phosphate (PO_4^{3-}), and a matrix protein analogue (Lacprodan, mOPN-10). This media composition delays premature precipitation of the calcium and phosphate in solution, allowing amorphous calcium phosphate to penetrate individual collagen fibrils and nucleate intrafibrillarly, closely mimicking native mechanisms of bone mineralization as demonstrated in previous studies[38, 39]. As a result, the engineered matrix recapitulates both the composition and hierarchical organization of the native bone tissue.

Importantly, this engineered microenvironment supports the emergence of physiologically relevant bone cell phenotypes and their spatial organization entirely in the absence of exogenous osteoinductive supplements (**Figure 1a-b**). Osteoblasts embedded within the mineralized matrix undergo maturation and become entrapped within the calcified collagen. Subsequent addition of osteoblasts and macrophages in the lateral channels resulted in their lining the tissue interface, where the macrophages differentiated into osteoclasts in as little as 48 hours. Together, these features establish a self-organizing, physiologically relevant bone-like microenvironment governed by endogenous cell–cell and cell–matrix interactions encoded by the platform design.

We further demonstrate the feasibility of adapting the platform to model complex, vasculature-driven multicellular interactions by incorporating a perfusable, microvascular capillary network that interfaces with the mineralized bone-like matrix, thereby resulting in a multicellular system consisting of vasculature, osteocytes and osteoclasts. (**Figure 1b, Supplementary Movie 1**) Notably, quantitative analysis revealed no significant differences in total vessel length or area between mineralized and non-mineralized conditions, indicating that mineralization did not impair vascular morphogenesis (**Supplementary Figure S1**). Importantly, this modular approach enables the stepwise integration of relevant tissue components, such as vasculature, to facilitate investigations of how vascular cues contribute to bone physiology and disease progression.

To validate the formation of a bone-like matrix, we assessed nanoscale mineralization relative to non-mineralized control samples (NM). Clear differences in opacity were observed between the non-mineralized and mineralized samples by light microscopy (**Supplementary Figure S2a-b**), which were attributable to mineralization as verified by Alizarin red staining, which showed visible evidence of mineral deposition in the mineralized groups (**Figure 1c-d**). Scanning electron microscopy (SEM) analysis (**Figure 1e-f**) revealed significant differences in fiber structure between the groups, with distinct mineral deposits on the collagen fibers apparent in the mineralized (MIN) samples. Moreover, the collagen fibers in the mineralized matrices appeared visibly thicker and were accompanied by surface roughness (**Figure 1h**). These structural changes, however, were notably absent in the non-mineralized samples (**Figure 1g**), offering further evidence supporting successful incorporation of nanoscale mineral in the collagen matrix. Additionally, Fourier Transform Infrared Spectroscopy (FTIR) was performed to confirm the chemical composition of the mineralized matrix. The mineralized samples exhibited prominent peaks corresponding to expected apatite phosphate (1030, 600, and 560 cm^{-1}), carbonate (874 cm^{-1}), and amide bands (1649, 1553, and 1248 cm^{-1}), absent in the non-mineralized controls (**Figure 1k**). These findings align with patterns observed in native bone[38, 39, 40]. Quantitative analyses showed significantly higher mineral-to-matrix ratios (**Figure 1j**) and crystallinity indexes (**Figure 1i**) in mineralized samples compared to controls, and comparable mineralization relative to native bone[40], corroborating the ability of this model to replicate key properties of bone tissue at the nanoscale level.

169 In the physiological context of bone, osteoblasts secrete a dense collagenous matrix, termed
170 osteoid, which eventually mineralizes to entrap the cells, triggering their transition into
171 osteocytes[41]. To determine whether the mineralized matrix in our system supports this transition,
172 we first confirmed that the mineralized matrix did not affect the viability of human osteoblasts
173 over the 3-day mineralization process (**Supplementary Figure S2c-e**). Samples were fixed and
174 immunostained to evaluate osteocyte differentiation. In the mineralized groups, cells displayed
175 marked morphological remodeling consistent with osteocyte maturation, including elongated cell
176 bodies, increased aspect ratios, and the development of dendritic cytoplasmic extensions forming
177 an interconnected network (**Figure 2 and Supplementary Figure S3b**). In contrast, cells in non-
178 mineralized conditions retained a rounded morphology with limited projections, consistent with
179 an osteoblastic state (**Supplementary Figure S3a**). Mineralization also induced significant
180 changes in protein expression associated with osteocyte phenotype and function. Osteocalcin
181 (OCN), a marker of osteogenic maturation, and podoplanin (PDPN), a mechanosensitive protein
182 involved in dendritic process formation, were both upregulated under mineralized conditions
183 (Figure 2a-d, h-i), though not significantly. Furthermore, expression of sclerostin (SOST), a critical
184 marker of terminal osteocyte differentiation, was significantly higher in the mineralized group
185 (**Figure 2e-f,i**), and high-magnification imaging (**Figure 2g**) showed PDPN localization along
186 dendritic processes, supporting the establishment of intercellular connectivity. Together, these
187 findings indicate that the mineralized microenvironment promotes coordinated structural changes
188 and protein expression patterns consistent with osteocyte lineage progression [37, 42]. Collectively,
189 the elongation of the osteoblasts, the formation of dendritic extensions, and the upregulation of
190 mechanosensitive PDPN and SOST align with the phenotypic transition from osteoblasts to
191 osteocytes[43, 44]. When directly compared with cultures treated with classical osteoinductive
192 medium (OIM) for seven days, OCN and PDPN expression levels were not significantly different
193 between the mineralized and OIM groups, whereas SOST expression was significantly higher
194 under matrix mineralization than standard OIM supplementation (**Supplementary Figure S3c–**
195 **h**). These data indicate that matrix mineralization alone is sufficient to induce osteocyte-associated
196 protein expression at levels that are either comparable or better to biochemical osteoinduction,
197 while promoting a more pronounced increase in SOST. Together, these findings demonstrate that
198 the nanoscale mineralized matrix within our platform accelerates osteoblast-to-osteocyte transition
199 in the absence of exogenous osteoinductive supplements, accompanied by enhanced expression of

mechanosensitive markers[45]. The regulation of osteocyte differentiation in a significantly accelerated timeline represents an important step to provide the mechanical and cellular cues to prepare a bone-prototypical environment for remodeling.

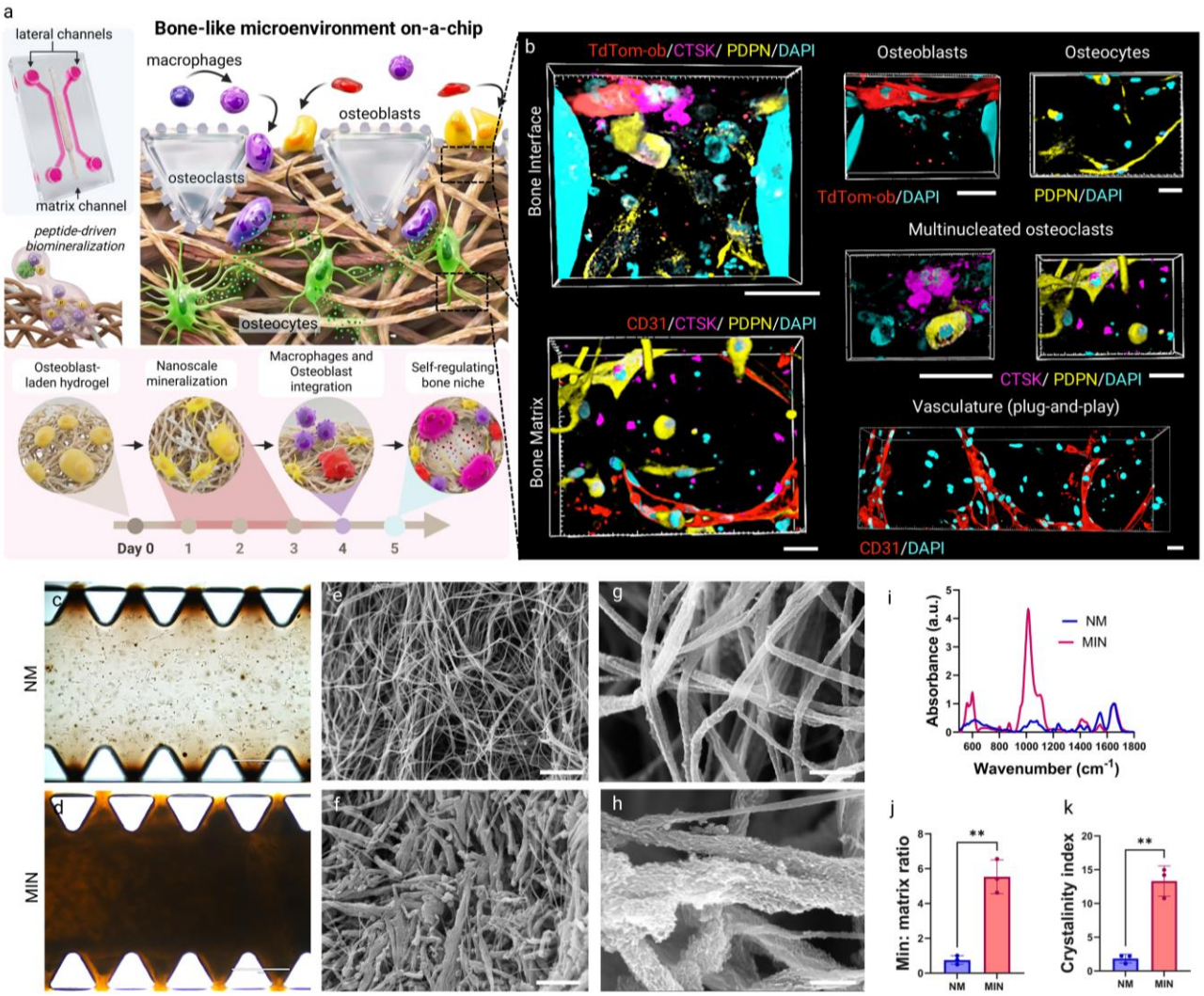

Figure 1. Bone-on-a-chip recapitulates the self-regulating multicellular complexity of bone within a mineralized matrix. (a) Conceptual schematic of the organ-on-a-chip platform illustrating the stepwise engineering of a mineralized bone-like microenvironment that establishes physiologically relevant spatial organization of bone cells and recapitulates key in-vivo interactions. (b) The engineered system enables the co-existence and direct interaction of osteoblasts (tdTom-ob; red), osteocytes (podoplanin, PDPN; yellow), macrophages, osteoclasts (cathepsin K, CTSK; purple), and vascular cells (CD31; red) without exogenous differentiation factors. Alizarin Red staining of non-mineralized (c) and mineralized (d) conditions demonstrates marked calcium deposition in mineralized samples. Scanning electron microscopy (SEM) at lower (e,f) and higher (g,h) magnification reveals the presence of discrete mineral nodules and increased apparent fiber thickness in mineralized (MIN) matrices compared to non-mineralized (NM) controls, consistent with mineral deposition within and around the fibrillar network. Fourier-transform infrared (FTIR) spectra (k), mineral-to-matrix ratio (j), and crystallinity index (i) further demonstrate increased mineral content

in mineralized groups. Experiments were performed with three biological replicates. Statistical significance in (f) and (g) was assessed by Student's t-test (**$p < 0.01$). Parts of this figure were created with BioRender.

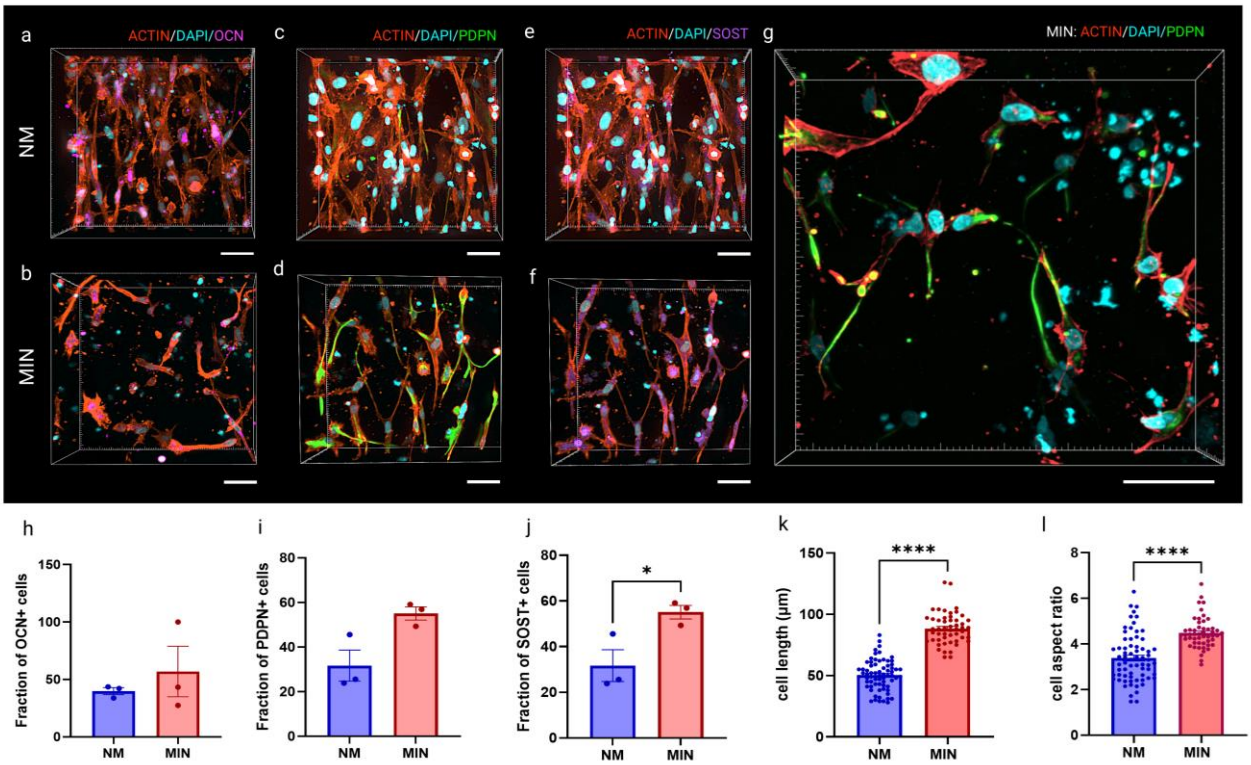

Figure 2. Bone-on-a-chip induces rapid osteoblast-to-osteocyte differentiation. Cellular morphology and lineage-specific marker expression were evaluated to assess osteoblast-to-osteocyte differentiation within the engineered microenvironment. Representative images (a–f) and corresponding quantifications (h–j) demonstrate increased expression of OCN and PDPN under mineralized conditions, with a statistically significant upregulation observed for SOST. Mineralized matrices exhibited cell-cell dendritic-like networks and pronounced PDPN localization (g), consistent with the acquisition of osteocyte-like features. Quantitative analyses of cell length (k) and aspect ratio (l) further revealed distinct morphological characteristics in mineralized relative to non-mineralized conditions, supporting accelerated osteoblast-to-osteocyte differentiation within the mineralized niche. Scale bars: 20 µm (a–g). Statistical significance was determined by a Student's t-test (****$p < 0.0001$; *$p < 0.05$).

2.2. Paracrine signaling accelerates functional osteoclastogenesis

Osteocytes play a central role in regulating bone homeostasis by coordinating the response of osteoblasts and osteoclasts through key signaling pathways. One of the key mechanisms regulating bone remodeling is the modulation of the ratio between receptor activator of nuclear factor κB ligand (RANKL) and osteoprotegerin (OPG)[46], where RANKL promotes osteoclastogenesis, and OPG serves as its inhibitor (**Figure 3a**). Osteocyte signaling, influenced by mechanical factors like matrix stiffness and fluid shear stress, bridges biomechanical and

236 biochemical cues, facilitating the recruitment of monocytes and their differentiation into
237 osteoclasts[47, 48]. While these interactions are well-characterized in-vivo, replicating them in-vitro
238 remains challenging, particularly when sustaining multiple differentiated cell types in culture using
239 exogenous growth factors alone, which can be difficult and lead to unintended crosstalk. In our
240 system, following matrix mineralization, during which osteoblasts matured into osteocytes, we
241 leveraged the resulting microenvironment to recreate the coordinated triad of bone cell activity
242 spatially. To do so, we introduced additional osteoblasts co-cultured with human monocyte-derived
243 macrophages, either isolated from patient peripheral blood or a human cell line, into the lateral
244 channel of the microfluidic chip. The added osteoblasts were intended to line the mineralized
245 matrix surface, supporting the differentiation of immune precursor cells into osteoclasts. This
246 configuration simulates the physiological recruitment of monocytes/macrophages to the bone
247 surface, where they undergo osteoclastogenesis in response to sustained osteocyte-derived cues
248 (**Figure 3a**). The osteoclast phenotype in mineralized chips was compared with control samples
249 either left untreated or treated with RANKL (50 ng/mL) and macrophage colony-stimulating factor
250 (M-CSF, 30 ng/mL), representing the traditional growth factor-mediated osteoclast differentiation
251 protocol (named NM + GF)[49].

252 A multiplex Luminex assay measuring a panel of cytokines and proteins revealed
253 significant differences in paracrine signaling profiles among the three groups over time. By day 3,
254 the mineralized samples demonstrated elevated levels of pro-osteoclastogenesis mediators such as
255 metalloproteinase 9 (MMP9), RANKL, and macrophage inflammatory protein 1 alpha (MIP-1α)
256 in comparison to both non-mineralized groups, while OPG production was significantly
257 downregulated (**Figure 3b**). Given the specific roles of RANKL and OPG in driving and inhibiting
258 osteoclastogenesis, respectively, this shift in the RANKL/OPG balance reflects transition to a pro-
259 osteoclastogenic state (**Figure 3b, Supplementary Figure S4 and Supplementary Figure S5**).
260 In mineralized groups, RANKL levels peaked at day 3 but returned to baseline by day 5, suggesting
261 a transient and tightly regulated osteoclastogenic response driven exclusively by embedded
262 osteocytes through crosstalk with osteoclast-precursor macrophages, in the absence of other
263 exogenous media supplements. On the other hand, RANKL and M-CSF-treated controls elicited a
264 pronounced and sustained pro-inflammatory response characterized by increased production of
265 TNF-α and IL-1β (**Figure 3b, Supplementary Figure S4 and Supplementary Figure S5**).
266 Importantly, our findings align with key mechanobiologically driven events described in-vivo

267 where matrix stiffness modulates RANKL/OPG signaling to drive osteoclastogenesis[50].
268 Additionally, the upregulation of macrophage inflammatory proteins (MIP) observed in the
269 mineralized groups further supports the physiological relevance of this model, given that these
270 chemokines are known to be involved in the recruitment of macrophages to the bone surface, which
271 is critical to initiate osteoclastogenesis[51].

272 In conventional 2D culture systems, osteoclastogenesis typically requires approximately
273 14 days or more of continuous RANKL/M-CSF stimulation. In contrast, incorporation of
274 biomechanical and paracrine bone cues directly secreted by primary bone cells embedded in a
275 mineralized matrix within our microengineered platform markedly accelerated this process. By
276 days 3 to 5, multinucleated osteoclasts derived from a human monocytic cell line expressed
277 cathepsin K, MMP9, and TRAP which were significantly more abundant in mineralized conditions
278 compared to non-mineralized controls, irrespective of exogenous RANKL and M-CSF
279 supplementation (**Figure 3c–k,m–p**). Supplementation of mineralized samples with RANKL and
280 M-CSF (MIN + GF) further increased the number of cathepsin K-, TRAP-, and MMP9-positive
281 multinucleated cells (**Supplementary Figure S6**), demonstrating the tunability of the system for
282 modeling graded and potentially individualized bone remodeling responses.

283 To determine whether this acceleration extended to primary human cells, we repeated the
284 experiments using monocytes isolated from peripheral blood mononuclear cells of healthy donors
285 (**Supplementary Figure S7a-c**). Following differentiation into macrophages ex-vivo, cells were
286 introduced into the lateral channels of the chips (**Supplementary Figure S7a**). Mineralized
287 conditions, with or without additional growth factors, induced significantly faster
288 osteoclastogenesis, as evidenced by increased numbers of cathepsin K- and MMP9-positive
289 multinucleated cells (**Figure 3l and Supplementary Figure S7d,e**). Elevated expression of these
290 resorptive enzymes in both cell lines and primary cells is consistent with enhanced osteoclast
291 differentiation and functional activation within the mineralized matrix.

292 Collectively, these findings demonstrate that the platform recapitulates a mineralized bone
293 niche that supports rapid and efficient osteoclastogenesis in both established cell lines and primary
294 patient cells. Of note, this effect is accompanied by local osteocyte–osteoclast modulation of the
295 RANKL/OPG axis, and occurs in the absence of prolonged growth factor–supplementation.

296

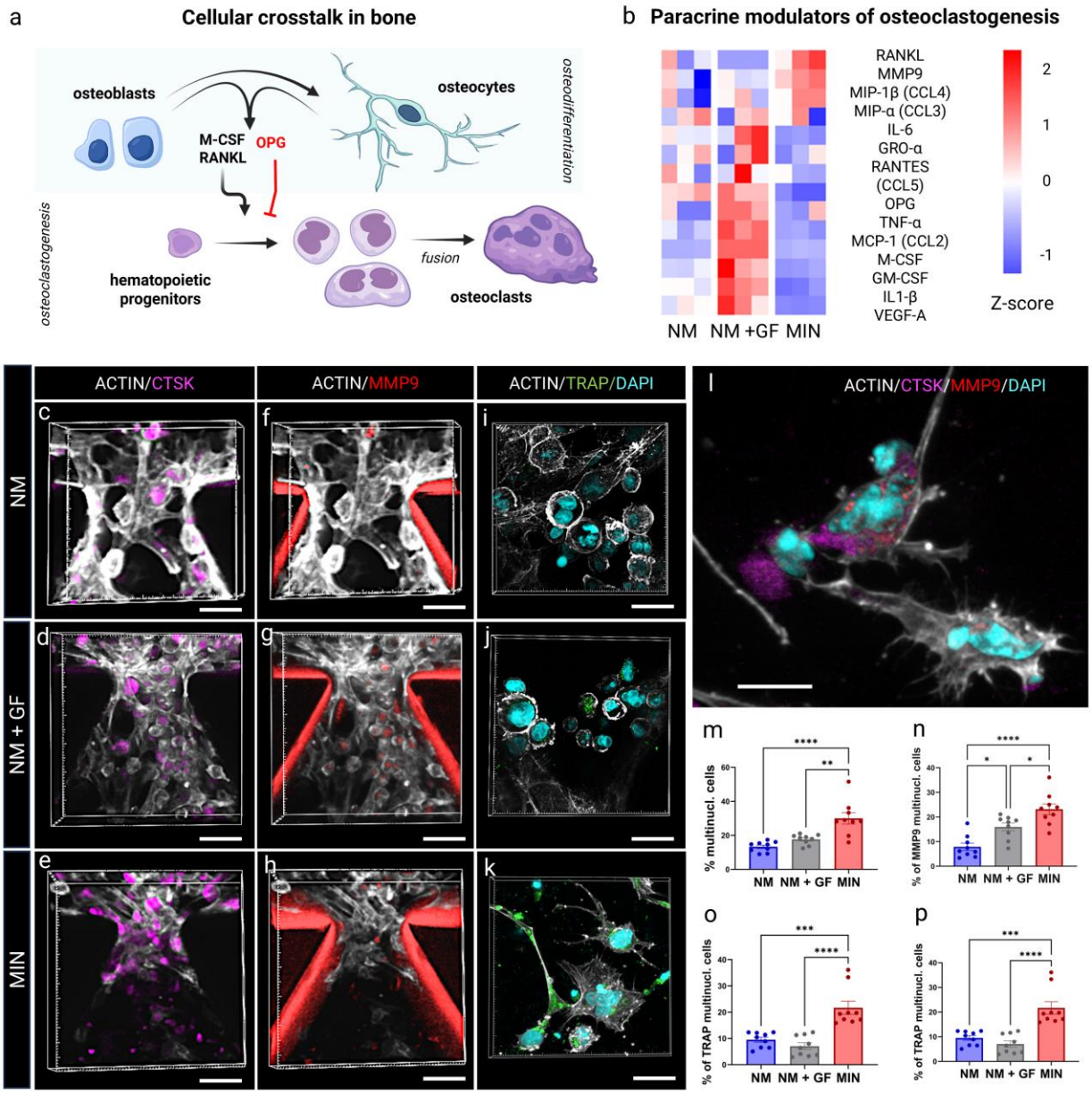

Figure 3. Paracrine signaling within the mineralized bone-on-a-chip drives rapid osteoclastogenesis. (a). Osteoblasts and macrophages were introduced into the lateral channel to model osteoclastogenesis mediated by osteoblast–osteocyte signaling, and culture supernatants were collected for analysis of osteoclastogenic factors. (b) Heatmap of secreted proteins measured by Luminex after 3 days of co-culture, shown as Z-scores, demonstrates increased RANKL and reduced OPG levels in mineralized matrices compared with non-mineralized (NM) matrices and non-mineralized matrices supplemented with RANKL and M-CSF (NM + GF). (c–k) Representative immunofluorescence images after 5 days of culture show cathepsin K (CTSK; magenta), (f-h) MMP9 (red), (i-k) TRAP (green), F-actin, and DAPI (blue), with mineralized matrices exhibiting increased multinucleation and characteristic osteoclast morphology relative to NM and NM + GF conditions. (l) Osteoclastogenesis was further validated using primary macrophages derived from peripheral blood mononuclear cells (PBMCs), which recapitulated multinucleated morphology and CTSK and MMP9 expression under mineralized conditions Quantification of multinucleated cells (m) and CTSK (n), MMP9 (o), and TRAP (p) expression measured specifically in multinucleated cells demonstrates significantly enhanced osteoclast differentiation in mineralized matrices. Scale bars: 50 µm (c–h)

312 and 30 µm (i–k, l). Experiments were performed with three biological replicates. Statistical significance was
313 determined by one-way ANOVA with Bonferroni correction (**p < 0.01, ***p < 0.001, ****p < 0.0001).
314
315
316 **2.3. Osteoclastogenesis through ECM-dependent pathways versus inflammatory**
317 **signaling**
318
319 To elucidate the molecular mechanisms underpinning the accelerated biomimetic
320 osteoclastogenesis observed in **Figure 3**, we performed targeted gene expression profiling to
321 compare differentiating cells exposed to mineralized versus non-mineralized matrices.
322 Osteoclastogenesis is classically regulated by the RANKL/RANK and M-CSF signaling pathways,
323 which converge on activation of NF-κB to initiate transcriptional programs associated with
324 osteoclast differentiation and activity[52]. While these pathways are well-characterized in 2D
325 cultures supplemented with exogenous RANKL and M-CSF, the signaling mechanisms engaged
326 by a mineralized matrix enriched with osteocyte-derived factors remain poorly explored in-vitro[49].
327 Our platform provides a unique opportunity to dissect these pathways as influenced by paracrine
328 crosstalk.

329 To evaluate how our engineered mineralized matrix compares to the traditional growth
330 factor-driven method of osteoclastogenesis, we compared the gene expression profiles of
331 osteoclast precursor macrophage cells cultured on biomimetically mineralized matrices with those
332 on standard collagen matrices supplemented with exogenous RANKL/M-CSF. RNA isolated after
333 three days of incubation was analyzed using a NanoString nCounter panel targeting a panel of 825
334 genes (**Supplementary Table 1**). Both groups exhibited enrichment of classical osteoclast
335 markers, such as *ACP5 (TRAP)* and *CTSK* (**Supplementary Figure S8**). However, inflammatory
336 genes such as *IL1B***,** *STAT1*, and *FSTL1* were significantly elevated in the RANKL/M-CSF treated
337 group, whereas genes related to cellular adhesion, migration, bone resorption, and ion homeostasis
338 were prominently upregulated in the mineralized matrix group (**Figure 4a**).

339 Focusing on a curated set of key osteoclast-related genes (**Figure 4c**), we observed marked
340 upregulation of matrix-modifying transcripts in the mineralized matrix group, including CTSK, a
341 key protease involved in bone matrix degradation (**Figure 4d**). These data suggest that mineralized
342 environments promote osteoclastogenesis through gene pathways that are mechanistically distinct
343 from the inflammatory signaling typically induced by RANKL/M-CSF treatment. Gene ontology

344 analysis of the top 100 upregulated genes in the mineralized matrix group further revealed
345 significant enrichment in cellular response pathways, cell-matrix adhesion, and cell migration
346 (**Figure 4b, Supplementary Figure S9**). The gene expression profiles in the mineralized
347 conditions were distinct from the growth factor culture conditions, which were enriched for
348 inflammatory mediators as reflected across principal component analysis, volcano plot, and gene
349 ontology comparisons (**Supplementary Figure S10-12**). Together, these findings highlight the
350 capacity of mineralized matrices to establish a physiologically relevant microenvironment that
351 supports osteoclast differentiation through adhesion- and matrix-mediated cues independent of
352 exogenous growth factor supplementation. This finding points to exciting possibilities in the field
353 of engineered models that have traditionally relied on supraphysiological supplementation of cells
354 with exogenous growth factors to stimulate biological activity, which, for the first time, we show
355 not to be necessary in the context of functional multicellular crosstalk in an engineered model.

356

357

358

359

360

361

362

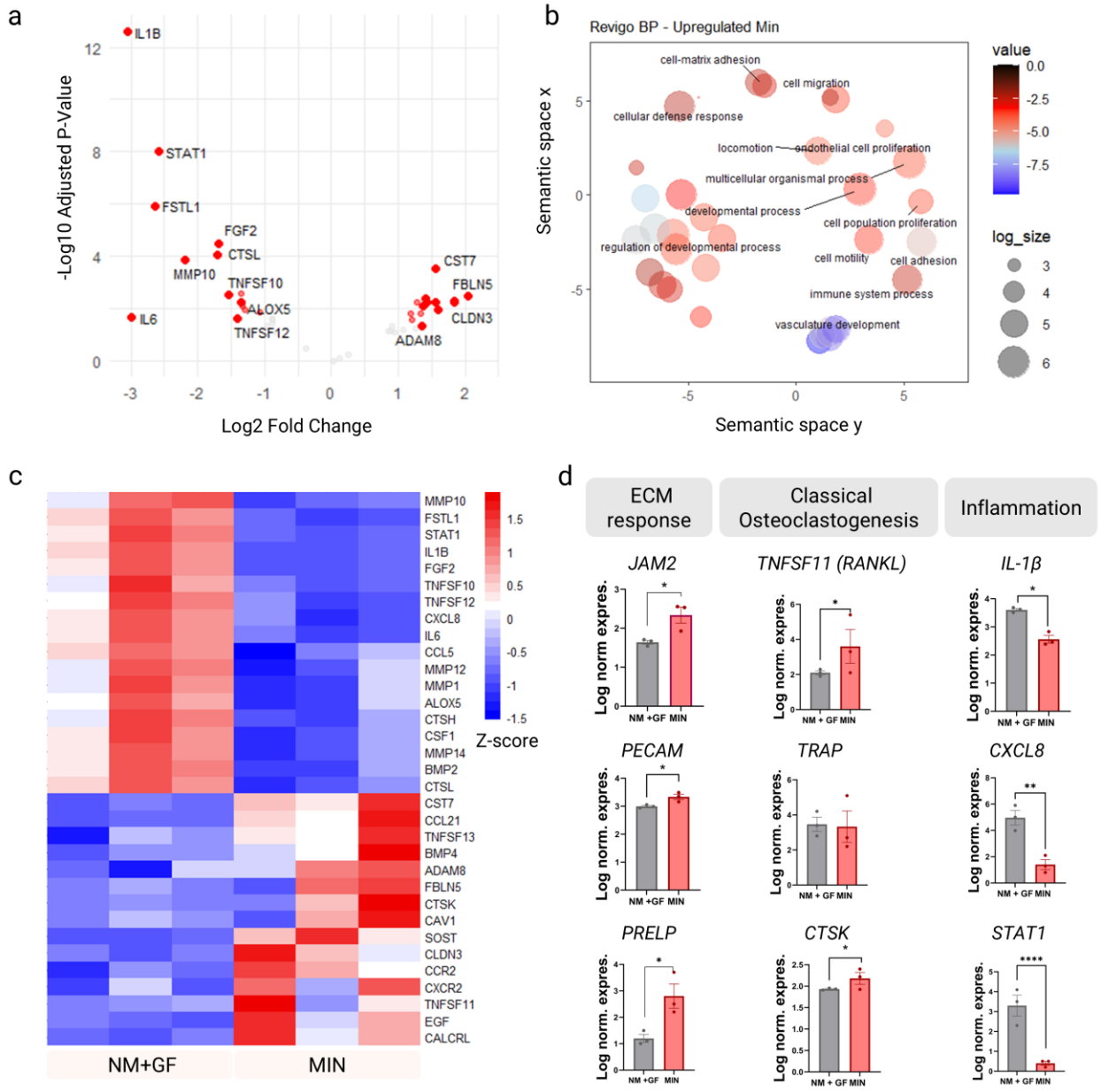

Figure 4. Distinct gene signatures characterize rapid biomimetic osteoclastogenesis in mineralized matrices. Osteoclasts differentiated within mineralized matrices (MIN) exhibit canonical osteoclast-associated gene expression profiles distinct from those observed in non-mineralized matrices supplemented with RANKL and M-CSF (NM + GF). (a) Volcano plot shows significantly differentially expressed genes from the 825-gene NanoString panel comparing MIN versus NM + GF, with each point representing log2 fold change and adjusted p-value; red points indicate significant differential expression. (b) A semantic similarity network generated using ReviGO, based on Gene Ontology (GO) terms enriched among the top 100 upregulated genes in MIN relative to NM + GF, highlights biological processes associated with osteoclast differentiation and matrix remodeling. GO enrichment analysis was performed using the Princeton GO Term Finder, and biological process terms with $p < 0.1$ are shown. (c) Heatmap displaying the average expression of significantly altered osteoclast-related genes across all replicates, with red indicating higher and blue lower expression; each column represents an individual replicate (n = 3 per condition). Log2 fold change of selected genes upregulated in MIN (d) is shown grouped by functional categories, including extracellular matrix response, canonical osteoclast markers, and inflammatory response; genes were selected from the NanoString panel

377 based on literature curation. Experiments were performed with three biological replicates. Statistical significance was
378 assessed by unpaired Student's t-test (**$p < 0.01$, ****$p < 0.0001$).

379

380 ## 2.4. Functional osteocyte-osteoclast responses to anti-resorptive therapies

381 Next, to evaluate whether our platform supports the functional response of osteoclasts from
382 precursor cells, we compared mineral degradation on mineralized samples engineered with and
383 without monocyte-derived macrophages. Bone resorption was assessed by quantifying pit areas
384 using second harmonic generation (SHG) imaging and by visualizing mineral degradation with
385 microCT (**Figure 5a-d and Supplementary Figure S13**). These analyses revealed a marked
386 increase in matrix degradation on chips containing osteoclasts compared to control groups lacking
387 osteoclasts, confirming robust osteoclastic activity. Notably, this dynamic, quantifiable level of
388 resorption has not previously been demonstrated using radiologic (μCT) methods in an on-a-chip
389 setting. We further evaluated the functionality of osteoclasts differentiated in the chip by
390 comparing their bone-resorbing ability to that of conventionally differentiated osteoclasts.
391 Osteoclasts retrieved from the chip were seeded onto calcium phosphate-coated resorption plates
392 and assessed for pit-forming activity over three days. Pit areas were comparable between chip-
393 derived osteoclasts and those differentiated using exogenous RANKL and MCS-F
394 (**Supplementary Figure S14**), further indicating that osteoclasts matured on-a-chip retain
395 functional bone-resorptive capacity even after removal from the device.

396 The inability of existing in-vitro models to capture key features of the bone
397 microenvironment undermines their predictive power for evaluating anti-resorptive drugs. To
398 establish our bone-on-a-chip system as a high-fidelity platform for preclinical drug testing, we
399 evaluated the effects of two clinically available anti-resorptive agents: alendronate, a
400 bisphosphonate, and denosumab, a monoclonal antibody targeting RANKL. Both drugs are widely
401 utilized in the treatment of osteoporosis and bone metastases, although clinical evidence
402 consistently indicates denosumab's superior efficacy[53]. Replicating these differential outcomes in-
403 vitro has been challenging due to the distinct mechanisms of action of these drugs and their reliance
404 on complex microenvironmental contexts. Denosumab inhibits osteoclastogenesis by binding to
405 RANKL, thereby disrupting signaling along the osteoblast-osteocyte-osteoclast axis[54]. In contrast,
406 alendronate is internalized by osteoclasts after binding to hydroxyapatite and interferes with
407 cytoskeletal organization[55]. Importantly, these mechanisms are modulated by osteocyte-mediated

signaling within a mineralized matrix, an element largely absent in conventional in-vitro models, such as calcium phosphate-coated resorption plates. To capture this complexity, macrophages were introduced into the bone-on-a-chip system after a 3-day mineralization period, followed by treatment with either alendronate (10^{-7} M) or denosumab (30 μg/mL) for 5 days. Samples were fixed and analyzed for cellular morphology, multinucleated cell formation, tartrate-resistant acid phosphatase (TRAP) expression, and functional osteoclast activity. Results were benchmarked against commercial calcium phosphate (CaP)-coated plates, which represent an industry-standard model of osteoclastogenesis using RANKL and MCS-F. Both drugs effectively suppressed osteoclastogenesis, as evidenced by a reduction in TRAP-positive multinucleated cells on both the chip and CaP plates (**Figure 5e-j**). However, only on-chip assays assessing matrix resorption revealed a significant difference in drug efficacy that matches the reported clinical efficacy of these drugs. Accordingly, on-chip experiments showed that denosumab significantly reduced bone resorption with smaller pit areas relative to both untreated controls and alendronate-treated samples. Experiments off-chip did not recapitulate these clinically reported results (**Figure 5l-q**), highlighting the sensitivity of the bone-on-a-chip model in comparison to established methods.

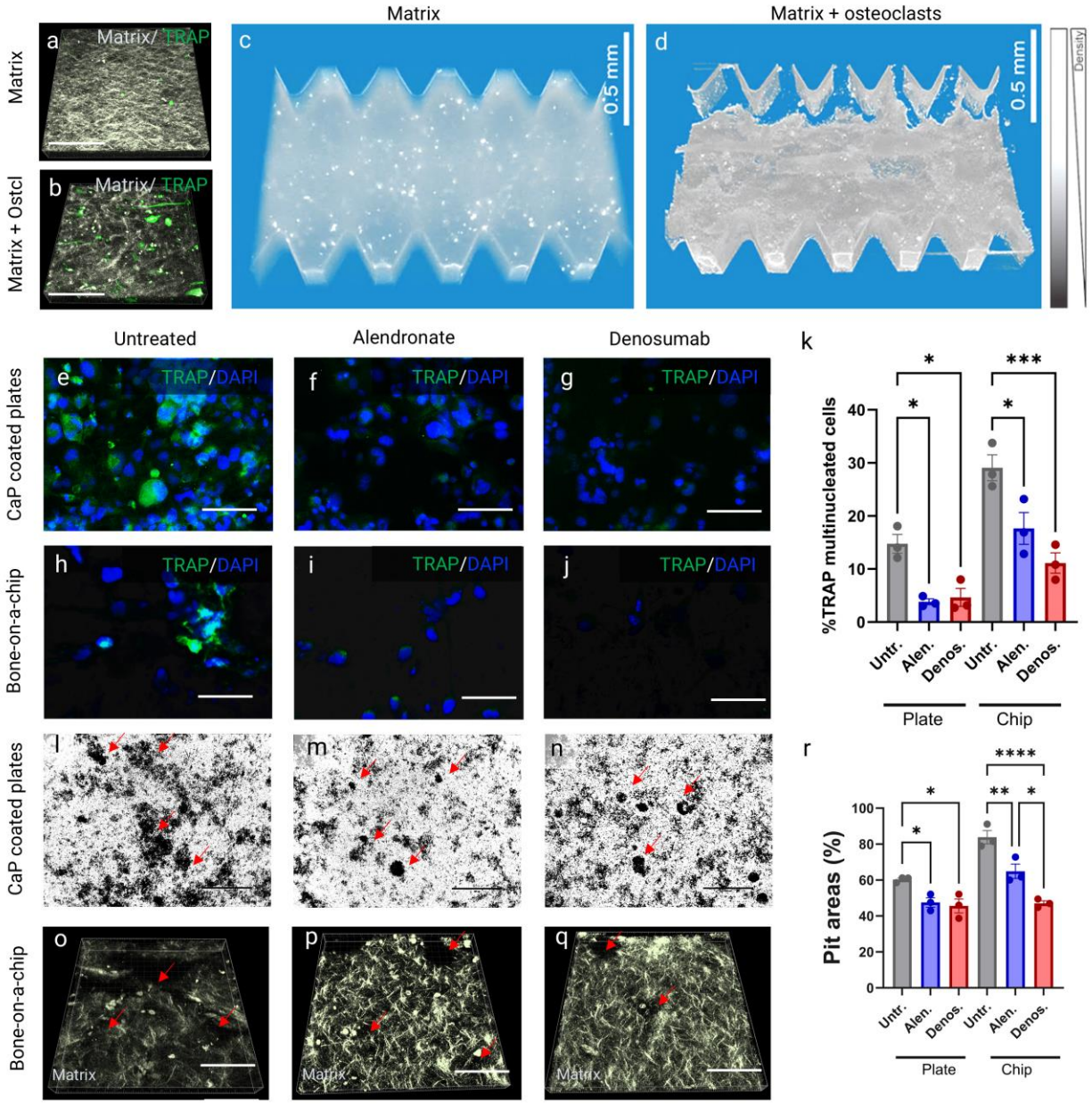

Figure 5. Mineralized bone on-a-chip enhances functional osteoclast activity and drug responsiveness. Second harmonic generation (SHG) microscopy of matrix-only (a) and matrix with osteoclasts (b) demonstrates resorption-associated matrix disruption in the presence of osteoclasts. Cross-sectional and lateral microCT reconstructions of mineralized matrices cultured with (c) or without (d) osteoclast exposure further reveal structural alterations consistent with matrix resorption. Representative TRAP staining of multinucleated osteoclasts formed on CaP-coated plates (e–g) or within the bone-on-a-chip platform (h–j) following treatment with vehicle, alendronate (10^{-7} M), or denosumab (30 μg mL^{-1}) shows reduced osteoclast formation with both anti-resorptive agents. Quantification of TRAP-positive multinucleated cells (k) confirms suppression of osteoclast differentiation across both platforms. Resorption pits are visualized in grayscale on CaP-coated plates (l–n) and by quantified via SHG imaging on-chip (o–q), with red arrows indicating pit regions. Quantification of pit area (r) demonstrates significant inhibition by both drugs; notably, the chip platform distinguishes differential effects between alendronate and denosumab. Data represent mean ± s.e.m. from

three biological replicates. Statistical significance was determined by one-way ANOVA with Bonferroni correction (*$p < 0.05$, **$p < 0.01$, ***$p < 0.001$, ****$p < 0.0001$). Scale bars: 100 µm (b, c, e–j, o–q) and 400 µm (l–n).

2.5. Recapitulating the invasion of oral cancer cells into bone

To evaluate the ability of the bone-on-a-chip system to model complex, disease-relevant phenomena that depend on cross-communication between heterogeneous bone-resident cell populations (**Figure 6a**), a challenge that remains difficult to address in-vitro, we investigated oral squamous cell carcinoma (OSCC) invasion into bone, a common and devastating process responsible for extensive bone destruction in oral cancer. Different from metastatic cancers, bone invasion occurs via cell infiltration into the matrix, as opposed to via vascular or lymph dissemination. While osteoclasts are known to facilitate bone invasion via paracrine signaling, existing in-vitro models fail to replicate the spatial and histological complexity observed in-vivo[56]. To address this gap, we compared OSCC invasion dynamics in engineered microenvironments with or without osteoclasts. Following osteoclast differentiation in the bone-on-a-chip system as described above, OSCC cells were seeded into one of the lateral channels of the microfluidic device after 3 days and co-cultured with bone cells (osteoblasts and pre-osteoclasts) for 24h. Invasion was then evaluated in the presence or absence of osteoclasts. Pan-cytokeratin (PanCK) staining was used to identify PanCK positive OSCC cells and visualize their spatial distribution relative to the mineralized matrix over time (**Figure 6b-c**). We found significantly lower numbers of $PanCK^+$ cells in the lateral channels in the groups containing osteoclasts (**Figure 6d**). In constructs where osteoclasts where not present, $PanCK^+$ OSCC cells appear largely localized along the mineralized matrix interface with limited penetration into the tissue (**Figure 6b, e–f**). On the other hand, in osteoclast-containing samples, $PanCK^+$ OSCC cells were detected beyond the invasive bone interface, deeper into the regions between pillar of the device (**Figure 6g**), These regions coincided with osteoclast-mediated matrix disruption and cavity formation, as evidenced by localized loss of collagen signal in SHG imaging (**Figure 6h**). In contrast, the mineralized matrix cultured with OSCC cells in the absence of osteoclasts remained largely intact with limited cancer invasion (**Figure 6f**), thus mimicking the known osteoclast mediation of oral cancer invasion occurring clinically.

Histological analysis using H&E staining, together with corresponding immunofluorescence sections (PanCK/Vimentin/DAPI), further confirmed OSCC penetration into the mineralized matrix and demonstrated deeper, spatially heterogeneous tumor cell localization in the presence of osteoclasts (**Figure 6i–n**). To further quantify invasion into the matrix, we measured the maximal perpendicular distance of $PanCK^+$ cells from the matrix interface and normalized this value to total matrix thickness to account for construct variability (**Figure 6m**). Although the difference in mean invasion depth did not reach statistical significance in a linear mixed-effects model ($p = 0.117$), distributional analysis revealed a significant rightward shift in invasion depth under osteoclast-containing conditions (KS test statistic = 0.75, $p = 0.013$) with increased variance in normalized invasion depth (Levene's test, $F = 6.09$, $p = 0.028$), indicating greater heterogeneity of invasion behavior. These results demonstrate that our bone-on-a-chip system faithfully replicates critical aspects of the OSCC-bone interface, offering a robust platform to dissect previously inaccessible questions in OSCC pathobiology, such as the earliest initiation events of bone invasion.

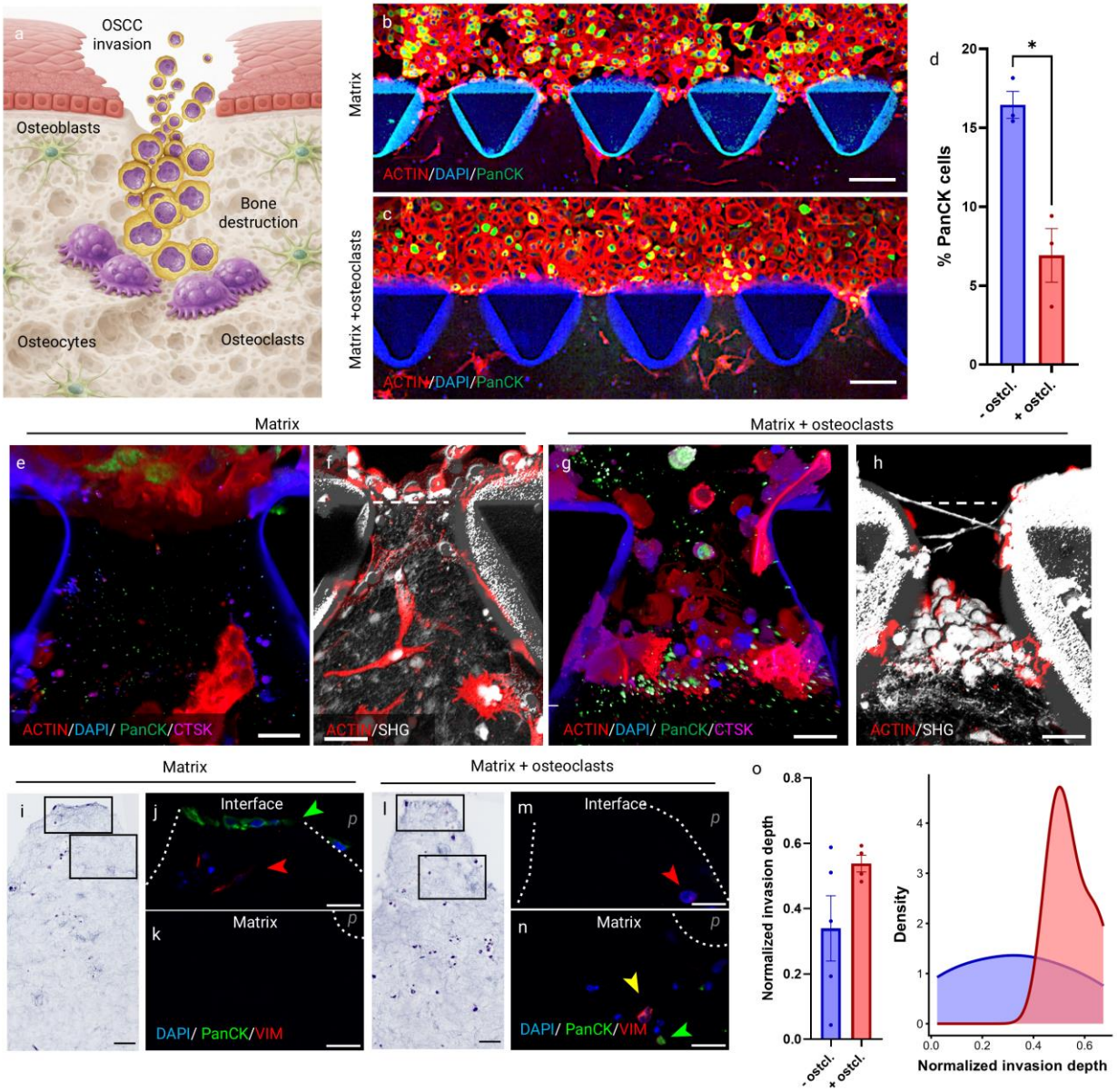

Figure 6. Bone-on-a-chip recapitulates key cellular and spatial hallmarks of OSCC bone invasion. OSCC cells were introduced into the lateral channels following establishment of the mineralized bone compartment, and invasion was assessed in the presence or absence of osteoclasts to model OSCC-associated bone invasion (a). Representative images show Pan-cytokeratin–positive OSCC cells (PanCK; green) distributed along and within the mineralized matrix in matrix-only (b) and matrix + osteoclast (c) conditions. Quantification (d) shows a significantly lower proportion of PanCK-positive OSCC cells located within the lateral channels in the presence of osteoclasts. High-magnification images of the tumor-matrix interface in matrix-only constructs without osteoclasts (e-f) and matrix + osteoclast constructs (g-h) demonstrate more pronounced matrix disruption and cavity formation in osteoclast-containing conditions. Immunofluorescence images (e,g) show ACTIN/DAPI/PanCK/CTSK, and corresponding second harmonic generation (SHG) imaging (f, h) reveals localized collagen degradation. Hematoxylin and eosin (H&E)–stained sections from matrix-only (i) and matrix + osteoclast (l) constructs, with corresponding immunofluorescent sections (j-k and m-n; DAPI/PanCK/VIM) further confirm OSCC penetration into the mineralized matrix. Osteoclast-containing conditions exhibit deeper and more heterogeneous PanCK^{+} cell (green arrowheads) invasion relative to matrix-only controls. Quantification of normalized invasion depth (o) shows no significant difference in mean invasion depth between groups; however, distributional analysis reveals a rightward shift and

494 increased variance in invasion depth in osteoclast-containing constructs. Scale bars: 100 μm (b, c); 50 μm (e-h); 25
495 μm (j-k, m-n). Statistical significance was determined by Student's t-test (*$p < 0.05$).

496

497 ## 3. Discussion

498 Recent advances in bone tissue engineering, particularly in bone-on-a-chip platforms, have
499 significantly improved our ability to model aspects of bone biology in-vitro[35, 57]. However,
500 recreating a self-regulated system that supports rapid osteocyte differentiation, osteoclastogenesis,
501 and vascularization within a 3D homogeneously calcified microenvironment, and without
502 exogenous growth factors, remains a fundamental obstacle in skeletal in-vitro models[58]. To address
503 this limitation, we demonstrate that engineering essential biomechanical and biochemical cues,
504 specifically nanoscale mineralization and embedded osteocyte networks, drives spontaneous and
505 rapid osteoclastogenesis that mirrors hallmark features of bone remodeling. Moreover, the
506 platform can be engineered to incorporate additional bone components, such as embedded vascular
507 capillaries supported by stem cell-derived pericytes, enabling selective addition or removal of key
508 cellular and matrix features that define bone function. Remarkably, in the absence of exogenous
509 osteogenic factors, osteoblasts embedded within a mineralized matrix matured within three days,
510 forming interconnected cellular networks and upregulating canonical osteocyte markers, including
511 PDPN. As shown in **Figure 2**, this biomimetic osteocytic differentiation represents a key milestone
512 in reproducing the physiological dynamics of bone remodeling and exceeds the capabilities of
513 existing 3D or on-chip bone models. PDPN, a transmembrane glycoprotein, is typically induced
514 when osteoblasts are subjected to mechanical stimuli within a mineralized environment and plays
515 a crucial role in establishing the osteocytic network by mediating dendritic connectivity[59].
516 Collectively, these findings establish that our engineered system recapitulates the osteoblast-to-
517 osteocyte transition in-vitro, capturing essential features of bone physiology and remodeling.

518 Our study establishes a self-regulating microenvironment that supports autonomous
519 osteoclastogenesis[60] mediated by multitypic cell-cell communication. The observed upregulation
520 of RANKL and MMP9, alongside suppression of OPG, reflects intrinsic paracrine signaling
521 between bone-forming and bone-resorbing cells, modulating osteoclast differentiation and activity.
522 This signaling cascade, initiated by matrix mineralization and the presence of embedded
523 osteocytes, supports rapid formation of multinucleated osteoclasts and functional bone resorption,

524 as validated by pit formation assays. Notably, macrophages differentiated into osteoclasts in the
525 absence of exogenous growth factors and localized specifically to the mineralized matrix zones,
526 suggesting effective niche recognition and activation. Cell fusion events were observed within
527 hours, highlighting the efficiency and fidelity of this model in recapitulating physiological
528 osteoclastogenesis. These findings are consistent with prior reports linking increased matrix
529 stiffness to enhanced osteoclastogenesis, evidenced by the upregulation of canonical markers such
530 as CTSK**,** MMP9, and ACP5[48, 61]. However, in contrast to conventional in-vitro systems that rely
531 on supraphysiological levels of RANKL and M-CSF, our platform leverages osteocyte-derived
532 cues to induce osteoclastogenesis. This physiologically relevant approach uncovered adhesion and
533 junction-associated genes as potential regulators of osteoclast differentiation, features previously
534 underappreciated[62]. Notably, genes such as *FBLN5***,** *CLDN3*, and *ADAM8* were significantly
535 upregulated in the mineralized condition, suggesting a matrix-dependent transcriptional program.
536 *FBLN5* was particularly noteworthy for its dual role in promoting *RANKL* expression while
537 suppressing osteogenic signaling, potentially acting as a molecular switch favoring
538 osteoclatogenesis[63]. *CLDN3*, a tight junction protein, may influence osteoclast-matrix interactions
539 by modulating cell adhesion dynamics[64]. Elevated *ADAM8* expression, a known mediator of
540 osteoclast precursor fusion, further supports its essential role in matrix-guided osteoclastogenesis,
541 since inhibition of *ADAM8* has been shown to markedly impair osteoclast formation[65]. By contrast,
542 samples treated with RANKL/M-CSF exhibited a transcriptional profile dominated by
543 inflammatory mediators, including pronounced elevation of *IL1B, CXCL8 and STAT1*, in
544 alignment with Luminex cytokine profiling (**Figure 3b and Supplementary Figure S5**). This
545 divergence highlights two possible distinct regulatory gene-associated pathways for osteoclast
546 differentiation - one driven by inflammatory cues under exogenous stimulation, and another by
547 matrix-embedded biophysical and paracrine signals orchestrated by osteocytes in a mineralized
548 environment. It is important to emphasize that this observation is based on a limited gene
549 expression snapshot, highlighting the necessity of further validation across wider regulatory
550 pathways.

551 The translational utility of our platform is illustrated by its ability to model therapeutic
552 responses with high fidelity, capturing clinically observed outcomes in-vitro. Clinical trials have
553 consistently shown that denosumab outperforms other antiresorptives in increasing bone mineral
554 density and reducing fracture risk[53], yet recapitulating these effects in-vitro has proven difficult.

555 Our system not only reflects these therapeutic trends but also establishes a robust preclinical
556 framework for evaluating bone-targeted drugs. Importantly, most in-vitro models lack both
557 osteocytes and the complete osteoblast-osteoclast-osteocyte axis of cellular crosstalk, often also
558 excluding vascular or chemechanical cues modulating drug response, especially calcium and
559 phosphate nanoscale minerals infiltrating collagens that cells bind and respond to. This omission
560 limits mechanistic insight, particularly as osteocytes regulate bone remodeling through the
561 RANKL/OPG signaling axis[66]. For example, the effects of alendronate on osteocyte biology
562 remain poorly defined, despite its widespread clinical use[67]. Similarly, denosumab's suppression
563 of RANKL activity elevates OPG and halts resorption[68]; however, this sustained suppression may
564 underlie the rebound bone loss observed after treatment discontinuation[69], a phenomenon that
565 cannot be investigated in osteocyte-deficient models. By enabling integrated readouts across cell
566 types within a physiologically mineralized biomimetic matrix, our platform provides a uniquely
567 sensitive system for dissecting drug mechanisms, dose-response dynamics, and treatment
568 withdrawal effects. Moreover, its modular design permits the incorporation of patient-derived
569 cells, laying the groundwork for personalized medicine approaches in bone disease therapy.

570 Beyond its capacity to model resorption, our platform offers a unique opportunity to
571 interrogate broader roles of osteoclasts in bone regeneration, osteocyte-mediated signaling, and
572 cancer-bone interactions, including tumor invasion and metastasis[70, 71, 72]. One clinically
573 significant application demonstrated here is the modeling of oral squamous cell carcinoma (OSCC)
574 invasion, a process that targets mineralized tissues and contributes to catastrophic bone loss in oral
575 cancer. Despite being the sixth most prevalent cancer worldwide[73, 74], oral malignancies remain
576 underrepresented in the development of advanced in-vitro models. Our system successfully
577 recapitulates osteolytic behaviors characteristic of OSCC bone invasion, capturing for the first
578 time in-vitro the spatial and cellular features observed in patient samples. This capability enables
579 dynamic monitoring of tumor-bone interactions, which have historically been limited to static,
580 end-point observations in-vivo. While prior studies have described bone invasion across multiple
581 cancer types[56, 75, 76], fundamental questions remain regarding the mechanisms driving OSCC
582 tropism toward bone. For instance, it was observed that OSCC cells exhibited morphological
583 transitions at the tumor-bone interface, suggestive of a potential epithelial-to-mesenchymal
584 transition (EMT), triggered by biophysical and biochemical cues from the mineralized matrix[77,
585 78,79], highlighting the relevance of our system for dissecting the early steps of cancer cell adaptation

586 to the bone microenvironment. Quantitative analysis of invasion depth revealed that osteoclast
587 induced a significant redistribution of invasion behavior, characterized by a rightward shift in the
588 depth distribution and increased variance. This pattern suggests that osteoclast-mediated matrix
589 remodeling does not uniformly enhance invasion across the tumor population but rather generates
590 permissive microenvironments that enable deeper penetration by a subset of OSCC cells. Such
591 heterogeneity mirrors clinical observations in which bone invasion often occurs through focal
592 osteolytic niches rather than diffuse infiltration. The ability of our platform to resolve these
593 distributional changes highlights the importance of modeling spatially organized multicellular
594 interactions within a mineralized context.

595 Despite these advances, certain limitations remain. The current model does not yet
596 incorporate components of the adaptive immune system, such as T and B lymphocytes, which are
597 known to influence both bone remodeling and tumor progression[80]. Additionally, while vascular
598 and neural elements have previously been integrated into our mineralized matrix platform[38],
599 further optimization is needed to address specific biological questions before these features can be
600 systematically included in disease contexts. Incorporating these components will expand the
601 model's utility for studying immune-mediated bone disorders and further enrich the complexity of
602 the tumor microenvironment. Looking ahead, the vascularized architecture of our model offers a
603 promising foundation for investigating perfusion dynamics, immune cell trafficking, and
604 mechanisms of metastatic dissemination within a controlled, bone-like microenvironment. With
605 its modular, plug-and-play design, this versatile platform is well-suited for studying bone biology
606 across both physiological and pathological states, spanning development, homeostasis, and
607 disease.

608 In summary, our biomimetic bone-on-a-chip model constitutes a significant advance in
609 tissue-engineered New Approach Methodology (NAM) platforms for bone research. By
610 recapitulating the structural, cellular, and biochemical intricacies of native bone, this system offers
611 an unprecedented opportunity to investigate bone physiology, model disease progression, and
612 evaluate therapeutic responses under physiologically relevant conditions. Its modular architecture
613 and biological responsiveness position it as a versatile tool for both fundamental research and
614 translational applications. As such, this innovation holds strong potential to accelerate the
615 development of precision therapies and deepen our understanding of skeletal pathophysiology

616 across diverse clinical contexts. More broadly, it marks a critical step toward the realization of
617 high-complexity in-vitro human models capable of complementing – or even replacing - animal
618 models in the pursuit of mechanistic insights and human-relevant therapeutic discovery.

619 # 4. Methods

620 **Cell Culture**

621 Human osteoblasts hFOB 1.19 (ATCC, CRL-3602) were cultivated in human osteoblast media
622 (Cell applications) supplemented with 10% fetal bovine serum (FBS) (Thermo Fisher) and 1%
623 Penicillin/Streptomycin (P/S) (Thermo Fisher). The cells were used in passages 6-12. Human
624 THP-1 monocyte cell lines (ATCC) were cultivated in Roswell Park Memorial Institute (RPMI
625 1640 media, Thermo Fisher) supplemented with 10% FBS, 1% P/S. Passages 10-15 were used to
626 ensure consistent differentiation capacity. THP-1 cells were differentiated into macrophages by
627 adding a solution of Phorbol 12-myristate 13-acetate (PMA, Sigma-Aldrich) (100 ng/mL) for 48h.
628 Human umbilical vein endothelial cells (Lonza) were cultured in Vasculife VEGF Endothelial
629 complete media (EGM, Lifeline Cell Technology CA). Human mesenchymal stem cells (hMSCs;
630 RoosterBio) were maintained in α-minimum essential medium (Gibco, Carlsbad, CA)
631 supplemented with 10% FBS and 1% P/S. Experiments utilized HUVECs and hMSCs between
632 passages 4 and 6. OSCC cells UCSF-OT-1109 (ATCC) were cultured in RPMI media
633 supplemented with 10% FBS and 1% P/S. Osteoblasts were transduced with *pEF1α-*
634 *tdTomato* lentiviral particles (Takara Bio) at a multiplicity of infection (MOI) of 5. Following
635 transduction, cells were selected with puromycin (1 µg/mL) to establish a stable tdTomato-
636 expressing population. All cells were maintained at 37 ºC in a humidified incubator with 5% CO_2.

637 **Microfluidic device and osteoblast-laden gel**

638 To establish the biomimetic tissue on a chip, we used a DAX-1 microfluidic device (AIM Biotech).
639 Each device contains a main channel (1.30 mm wide x 0.25 mm high) flanked by two secondary
640 media channels (0.5 mm wide x 0.25 mm high). Prior to gel loading, chips were coated with 1
641 mg/mL of poly-D-lysine (PDL; Merck) for three hours at 37°C to improve collagen adherence. To
642 prepare the osteoblast-laden hydrogel, acid-solubilized type I collagen from rat tail (3 mg/mL,
643 Thermo Fisher) was diluted to a final concentration of 2.5 mg/mL in 10x phosphate-buffered saline
644 (PBS) with α-MEM media (Gibco, Thermo Fisher), neutralized with 1 N sodium hydroxide

645 (NaOH) to pH 7.4. The mixture was combined with a suspension of osteoblasts for a final
646 concentration of 3×10^6 cells/mL. A 10 µL volume of the resulting pre-gel solution was pipetted
647 into the central channel of each microfluidic device. The samples were maintained in a humidified
648 incubator at 37 °C for 45 min to allow self-assembly fibrillogenesis.

649 For vascularized constructs, a suspension containing hMSCS, HUVECs, and osteoblasts in a 4:1:1
650 ratio (final concentration of 18 mi cells/mL) was dispensed into the main channel of the chip (10
651 µL total volume). The cell mixture was embedded in a hydrogel composed of 2.5% collagen type
652 I, 2U/mL thrombin, and 1.25 mg/mL fibrinogen. The vessels were allowed to form for 2 days while
653 culturing in EGM prior to mineralization.

654 **Nanoscale mineralization**

655 To induce the collagen mineralization, a mineralizing medium was prepared containing 9 mM
656 $CaCl_2 \cdot 2H2O$ (J.T. Baker) and 4.2 mM K_2HPO_4 (J.T. Baker) in α-MEM supplemented with 10%
657 FBS and 1% P/S, based on our previously described protocol (REF). Lacprodan® OPN-10 (Arla
658 Foods Ingredients Group P/S), a bovine milk-derived osteopontin analogue, was added to the
659 $CaCl_2$-containing solution at a concentration of 100 µg/mL before the addition of K_2HPO_4. To
660 maintain a stable pH of 7.4, 25 mM HEPES was added to the mineralizing medium. The media
661 was added to the side reservoirs of the microfluidic chips and the devices were placed on a 2D
662 rocker platform inside a humidified incubator (37 °C, 5% CO_2, 95% humidity) to allow continuous
663 flow and homogeneous mineralization throughout the gel. The media was replaced daily for 3
664 consecutive days to allow full mineralization of the biomimetic bone-on-a-chip construct.

665 **Matrix characterization**

666 *SEM* **-** Mineralized and non-mineralized samples were fixed with 2% glutaraldehyde on a 2D
667 rocker at room temperature for 2 hours, followed by washing with distilled water. Samples were
668 dehydrated in an ascending ethanol series, removed from the chip, and subjected to critical point
669 drying. The dried samples were mounted, sputter-coated with a 10 nm platinum coating, and
670 imaged using a Helios Nanolab™ G3 DualBeam™ SEM (FEI, Thermo Fisher) (N = 3).

671 *FTIR* - Fourier Transform Infrared (FTIR) spectroscopy was performed using a Nicolet 6700
672 spectrometer (Thermo Scientific) in transmission mode. Spectra were recorded with 32 scans
673 across a range of 4000–400 cm^{-1}, with a resolution of 4 cm^{-1}. The mineral-to-matrix ratio was

674 determined by comparing the area of the ν_3PO_4 peak (1030 cm^{-1}) to that of the amide I peak (1660
675 cm^{-1}) after applying baseline correction and normalization to the amount of amide present. The
676 crystallinity index was assessed using the splitting factor, calculated from the doublet peaks in the
677 fingerprint region (500–650 cm^{-1}), primarily attributed to $\upsilon_4PO_4^{3-}$ bending vibrations. This
678 calculation involved summing the peak heights at 565 cm^{-1} and 605 cm^{-1} and dividing by the
679 height of the trough between them at 590 cm^{-1}. Peak height measurements were conducted using
680 Spectragryph software, with spectra normalized to the intensity of the amide I band (1585–1720
681 cm^{-1}) following baseline correction (N=3).

682 *Alizarin red* - An alizarin red assay was performed further to confirm the presence of calcium
683 deposition inside the hydrogel. The samples were stained with a 2% (w/v) alizarin red S solution,
684 incubated for 15 minutes, and then washed in water until the solution was clear. The stained areas
685 were analyzed by inverted microscopy (FL Autos, EVOS – Thermo Fisher Scientific) (N=3).

686 **Osteocyte characterization**

687 *Cellular viability* – After 3 days of mineralization, the cells inside the matrix were stained with a
688 Live/Dead Cell Imaging Kit (Molecular Probes, Thermo Fisher) to confirm their viability.
689 Following incubation, the specimens were washed with PBS and imaged using an inverted
690 fluorescence microscope (n = 3) (FL Autos, EVOS – Thermo Fisher Scientific, Waltham, MA,
691 USA). Image processing and analysis were performed using ImageJ (FIJI) software[81] to assess cell
692 viability, calculated as the ratio of total nuclei (blue, stained with 4′,6-diamidino-2-phenylindole,
693 DAPI) to dead cells (red, stained with Propidium Iodide).

694 *Comparison of mineralized matrix and osteogenic induction:* To compare the effects of the
695 mineralized matrix with conventional osteogenic induction, collagen-containing osteoblasts ($3 \times$
696 10^6 cells/mL) were either cultured for 3 days to allow matrix mineralization or treated with
697 osteogenic medium (100 nM dexamethasone, 50 μM ascorbic acid, and 10 mM β-glycerol
698 phosphate) for 7 days. PDPN expression was used as an immunofluorescent marker to assess
699 differences between conditions.

700 *Cell morphology and protein expression via immunostaining* - Samples (N = 3) were fixed in 10%
701 neutral-buffered formalin for 30 min at room temperature and washed three times with PBS. All
702 subsequent processing (including demineralization, permeabilization, blocking, antibody

703 incubations, and washes) was performed in a microwave-assisted system using the PELCO
704 Biowave Pro+ Tissue Processing System (Ted Pella, Redding, CA). Samples were placed on the
705 PELCO ColdSpot® temperature-controlled surface within the PELCO EM Pro microwave
706 vacuum chamber, sealed against the ColdSpot, and processed under a microwave power of 250 W
707 with a vacuum of approximately 20 mm Hg. The ColdSpot® surface was maintained at 10 °C
708 during demineralization, antibody infiltration, and wash steps, and at 21 °C during
709 permeabilization and blocking. Demineralization was performed in 10% (w/v) EDTA in PBS (pH
710 7.4). Primary antibodies were then applied under microwave-assisted diffusion. The following
711 primary antibodies were used: rabbit polyclonal anti-OCN (Bioss antibodies, bs4917R) (1:50
712 dilution), mouse monoclonal anti-PDPN (Origene, DM3500P) (1:100 dilution), and SOST (Bioss
713 bs-10200R 1:100 dilution). The following secondary antibodies were used at the specified
714 dilutions: Alexa Fluor 555 goat anti-mouse IgG (Thermo Fisher Scientific, A21422) (1:200
715 dilution) and Alexa Fluor 647 goat anti-rabbit IgG (Thermo Fisher Scientific, A21244) (1:200
716 dilution). After washing, the secondary antibody (Alpaca anti-mouse Alexa fluor 488 antibodies,
717 Jackson Laboratories, 615- 545- 214, 1:250 dilution) was applied using microwave-assisted
718 diffusion. F-actin was stained with 555-conjugated phalloidin (molecular probes, Thermo Fisher),
719 and nuclei were counterstained with DAPI (Thermo Fisher). Imaging was performed on a Zeiss
720 LSM 880 confocal microscope, and quantitative analyses of cell morphology and protein
721 expression were carried out with Imaris (v10.1, Oxford Instruments) and FIJI.

722 **Paracrine Signaling via Luminex**

723 Secreted cytokines and growth factors were quantified using a ProcartaPlex multiplex
724 immunoassay (Thermo Fisher), following the manufacturer's instructions. Supernatants were
725 collected from biomimetic bone-on-a-chip constructs after 1, 3, and 5 days of incubation under the
726 following conditions: (i) mineralized chips, (ii) mineralized chips treated with RANKL (50 ng/mL,
727 Peprotech) and MCS-F (30 ng/mL, Peprotech), and (iii) non-mineralized controls. The Luminex
728 assay targeted 14 analytes associated with osteoclastogenesis: MCP-1 (CCL2), OPG, VEGF, IL-
729 1β, GM-CSF, TNF-α, MIP-1β (CCL4), RANTES (CCL5), RANKL, M-CSF, MMP-9, GRO-α,
730 MIP-1α (CCL3), and IL-6. Samples were run on a Luminex 200 instrument (Thermo Fisher). The
731 analyte concentrations were determined by extrapolating individual experimental fluorescence
732 intensity values against each analyte's standard curve. The experiment was performed in three

733 biological replicates, and the results were reported as individual concentrations (pg/mL) and as Z-
734 scores for comparative heatmap visualization. For the groups treated with RANKL and M-CSF,
735 the analysis was adjusted by subtracting the baseline concentrations already present in the medium.

736 **Osteoclast characterization**

737 *THP-1 cells* –THP-1-derived macrophages were seeded onto chips and cultured for 5 days under
738 three conditions: (i) non-mineralized controls, (ii) non-mineralized chips supplemented with
739 RANKL (50 ng/mL) and M-CSF (30 ng/mL), and (iii) mineralized chips. After culture, samples
740 (N = 3) were washed with 1× PBS and fixed in 10% neutral-buffered formalin for 30 min at room
741 temperature. All subsequent steps, including decalcification with EDTA, permeabilization,
742 antibody incubations, and washes, were performed using a microwave-assisted system (PELCO
743 Biowave Pro+, Ted Pella, Redding, CA). Samples were placed on the PELCO ColdSpot®
744 temperature-controlled surface within the PELCO EM Pro microwave vacuum chamber, sealed
745 against the ColdSpot, and processed under a microwave power of 250 W with a vacuum of
746 approximately 20 mm Hg. The ColdSpot® temperature was maintained at 10 °C for antibody
747 infiltration and washing steps, and at 21 °C during permeabilization. Permeabilization was
748 performed with 0.1% Triton X-100, followed by three washes with PBS. Primary antibodies were
749 applied under microwave-assisted diffusion. The following primary antibodies were used: anti-
750 TRAP (Novus Biologicals, NBP2-45294, 1:100), anti-MMP9 (Bioss, bs-4593R, 1:100), and anti-
751 cathepsin K (Thermo Fisher, PA5-18950, 1:100). After washing, secondary antibodies were
752 applied using microwave-assisted diffusion: Donkey anti-goat Alexa Fluor 647 (705-607-003,
753 1:250 dilution), Donkey anti-mouse Alexa Fluor 790 (SA-000100, 1:250 dilution), and Alpaca
754 anti-mouse Alexa Fluor 488 (615-545-214, 1:500 dilution).

755 *Patient samples* - All coded human subject samples, including peripheral blood samples and data,
756 were obtained from the Cancer Early Detection Advanced Research (CEDAR) Specimen and Data
757 Repository (IRB#18048). Samples under the repository are collected from clinics across OHSU
758 following informed consent and released in accordance with the OHSU institutional review board.
759 At the time of sample collection, donors were not undergoing any therapies or treatments.
760 Peripheral blood monoclonal cells (PBMCs) were purified from whole blood over a Ficoll-Paque
761 PLUS (GE Healthcare) gradient and cryopreserved prior to analysis.

762 *Monocyte isolation* - Monocytes were isolated using the Stemcell Technologies Human Monocyte
763 Isolation Kit (Catalog# 19359). Briefly, PBMCs were thawed, washed and incubated with the
764 isolation cocktail. After incubation with magnetic particles, the CD14+ cells were enriched using
765 a magnet. CD14+ cells were counted and used for phenotyping and macrophage differentiation.

766 *Antibodies and flow cytometry* - On day 0 (prior to macrophage differentiation) and on day 7 (after
767 macrophages were differentiated with M-CSF 30 ng/mL - Peprotech), a small aliquot of cells was
768 stained to assess viability and cell surface marker expression. Cells were first incubated with a
769 fixable live/dead dye to distinguish viable cells (BioLegend, Zombie Yellow Fixable Viability Kit,
770 Catalog# 423104) and then stained with a combination of antibodies. Fluorescently labeled
771 antibodies used were as follows: CD11b APC/Fire 750, CD14 APC, CD68 PE-Cy7, CD80
772 BUV805, CD86 BB515 and HLA-DR BUV563. Cell-surface staining was performed in FACS
773 buffer (PBS supplemented with 1% FBS and 0.01% NaN3). Stained cells were acquired on the
774 Cytek Aurora spectral flow cytometer. Data was analyzed with FlowJo software, version 10.10.0
775 (Treestar).

776 Cell morphology was visualized with Alexa Fluor 555-conjugated phalloidin, and nuclei were
777 counterstained with DAPI (Molecular Probes, Thermo Fisher). Samples were imaged on a
778 CrestOptics X-Light V3 spinning disk confocal system (Nikon Ti2) and a Zeiss LSM 880 laser-
779 scanning confocal microscope (Fast Airyscan). Image analysis was performed with Imaris (v10.1,
780 Oxford Instruments) and FIJI (ImageJ) to quantify multinucleated cells (≥2 nuclei per DAPI
781 staining) and expression levels of TRAP, cathepsin K, and MMP9.

782 **Gene expression and quantification analysis**

783 Samples were collected from three conditions: either non-mineralized, non-mineralized and treated
784 with RANKL and M-CSF or mineralized. The lateral channels of each chip were washed with PBS
785 and treated with TRI reagent (Zymo Research) for RNA/DNA/protein isolation. Total RNA was
786 extracted and purified using the Direct-zol RNA MicroPrep kit (Zymo Research) following the
787 manufacturer's protocol. RNA concentration and purity were assessed using a Nanodrop One
788 spectrophotometer (Thermo Fisher). Only samples yielding at least 150 ng of RNA were utilized
789 for downstream analysis. A 1.5 µl aliquot of RNA lysate was used in the nanoString hybridization
790 reaction, and the remainder was stored at −80 °C. nCounter Elements (nanoString) hybridization
791 was performed according to the manufacturer's instructions. The Pan-Cancer Progression panel

792 was used, with the addition of a custom list of 55 bone-specific genes (see Dataset 1 for full gene
793 list). Differential gene expression analysis was performed using the R package DESeq2 (v 1.24.0).
794 Raw count data were normalized using DESeq2's median of ratios method, and differential
795 expression was assessed using the negative binomial generalized linear model (GLM). Genes with
796 an adjusted p-value < 0.01 and absolute fold change ≥ 2 were considered significantly differentially
797 expressed. Two differential gene lists were obtained by adjusting the p-value. Visualization was
798 performed using the heatmap (v1.0.12) R package, displaying the top 50 general genes and a
799 curated list of 33 osteoclast-specific genes. A volcano plot was generated using glMDPlot and
800 glXYPlot from the Glimma package (v1.10.1) to highlight differential expression between non-
801 mineralized + RANKL/M-CSF and mineralized conditions.

802 **Bone remodeling in-vitro**

803 *Calcium phosphate resorption assay* - Macrophages (THP-1 derived) were seeded at $1x10^5$ cells
804 per well in a 48-well calcium phosphate (CaP)-coated plate (Bone resorption assay plate,
805 AMSBIO) with RPMI media supplemented with10% FBS and 1% P/S. The control groups for the
806 experiment were: untreated macrophages (negative control) and a group treated with RANKL (50
807 ng/mL) and MCS-F (30 ng/mL) (positive control). After 12 days, we added osteoclasts
808 differentiated on the biomimetic bone-on-a-chip and cultured them further for 2 days. The plates
809 were then washed with PBS and deionized water, followed by 5 min of sodium hypochlorite,
810 according to the manufacturer's instructions. Subsequently, the samples were washed with DI
811 water again and dried out before being taken to a microscope (Evos FL auto 2, Thermo Fisher). Pit
812 areas were analyzed by ImageJ (images transformed into 8-bit and a threshold of 120 units) from
813 3 different biological replicates.

814 *Second harmonic generation microscopy* - Mineralized chip sample matrix structure was
815 compared in the presence or absence (control) of differentiated osteoclasts using second harmonic
816 generation microscopy (SHG). The samples were fixed and immunostained for TRAP as
817 previously described. The samples (N=3) were imaged using a laser-scanning confocal microscope
818 (Zeiss LSM 880) configured to capture the reflected light between 485 nm and 495 nm, after
819 exciting with a 900 nm laser. The 3D reconstruction was performed using Imaris 10.1 (maximum
820 intensity projection, ch1 channel min-164 and max 6251.69, gamma 1.00), and the analysis of

821 resorbed areas was performed by calculating the black (degraded tissue) to white (preserved tissue)
822 ratio areas in FIJI (images transformed into 8-bit and a threshold of 30 units).

823 *Mineral visualization by X-ray tomography* - For assessment of mineralized regions of the bone-
824 on-a-chip, the whole chip assemblies (n=3) were scanned via high-resolution X-ray tomography
825 at 2.3 μm resolution (Zeiss XRadia 620 Versa X-ray Microscope). Chips were scanned after
826 paraformaldehyde fixation (4%), rinsed in PBS, and sealed with Kapton tape. For visualization of
827 the high-resolution X-ray tomography scans, samples were placed at distances from the X-ray
828 source to produce the same energy intensity and resolution at the volume of interest. Scan settings
829 were held constant across all samples as follows: 70 kV voltage, 8.5 W power, 4X objective, 2X
830 binning, and 1-second exposure time. Images were transferred to Dragonfly Pro (Object Research
831 Systems) for visualization. Intensity values varied between scans due to differing amounts of chip
832 material remaining. For qualitative comparison, scans were window-leveled by adjusting the
833 minimum intensity threshold to exclude the plastic chip from view while preserving all higher
834 intensity values.

835 *Anti-resorption drug testing* - The most common anti-resorptive drugs, bisphosphonate
836 alendronate sodium (USP Reference standard, Sigma Aldrich, 10^{7} M) and the monoclonal anti-
837 RANKL biosimilar Denosumab (Research Grade, Ichorbio, 30 μg/mL) were chosen for our study.
838 Alendronate sodium was diluted in deionized water, and denosumab was diluted in PBS. The drugs
839 were added to the lateral channel following mineralization and prior to macrophage seeding. The
840 concentration used for alendronate was 10^{-7} M and for denosumab was 30 μg/mL. The media was
841 changed daily for 5 consecutive days, after which cellular viability was evaluated for both drug
842 conditions. The anti-osteoclastogenic effect of the drugs was determined by counting the number
843 of $TRAP^{+}$ and multinucleated cells in comparison with the untreated mineralized group. Osteoclast
844 inhibition by both drugs was determined by quantifying the extent of resorption in FIJI (ImageJ),
845 defined as the ratio of degraded (black pixels) to preserved (white pixels) tissue areas. The drugs
846 were also tested on Ca-P coated plates (in-vitro gold standard for osteoclast activity) at the same
847 concentrations to compare their osteoclast inhibitory effects for comparison with our biomimetic
848 model.

849

850

851 **OSCC bone invasion**

852 *2D experiments* – UCSF-OT-11 OSCC cells were cultured in RPMI supplemented with 10% fetal
853 bovine serum (FBS) and 1% penicillin/streptomycin (P/S) and used between passages 5–12. Type
854 I collagen disks (100 μL per disk; 12 mm diameter) were prepared in 24-well plates and
855 mineralized for 3 days using the mineralization medium described above. After mineralization, 5
856 × 10^4 OSCC cells were seeded onto mineralized collagen, non-mineralized collagen, or tissue
857 culture plastic controls and maintained for 3 days. Samples were then fixed with 4%
858 paraformaldehyde and processed for immunofluorescence staining using mouse anti–pan-
859 cytokeratin (Origene, TA190320; 1:1000) and rabbit anti-vimentin primary antibodies (NB1-
860 31327), followed by alpaca anti-mouse Alexa Fluor 488 (615-545-214; 1:500) and goat anti-rabbit
861 Alexa Fluor 647 (Thermo Fisher Scientific, A21244; 1:200) secondary antibodies. Fluorescent
862 images were acquired using an EVOS FL Auto imaging system (Thermo Fisher Scientific).
863 Experiments were performed in biological triplicate (N = 3).

864 *OSCC model* - For the OSCC bone invasion test, UCSF-OT-1109 cells were cultured in RPMI
865 supplemented with 10% FBS and 1% P/S in passages 5-12. Cancer cells (a total of $3x10^4$ cells)
866 were added into the lateral channel of the microfluidic chips that contained early osteoclasts (after
867 3 days of osteoclast differentiation). The co-cultures were maintained for 24h to allow paracrine
868 and direct interactions between OSCC cells and bone cells. Samples were fixed and
869 immunostained for markers for osteoclasts (cathepsin-k, Invitrogen PAS18950 1:100) and cancer
870 cells (pan-cytokeratin, Origene SKU TA190320, 1:1000) as previously described.

871 *Histological staining:* Tissue was fixed with 4% PFA for 45 minutes, then extracted from the
872 microfluidic device using 2% agarose. Samples were processed for standard formalin-fixed
873 paraffin-embedding by dehydration through a series of graded ethanols, xylene, and infiltration
874 with paraffin wax. Processed tissue was embedded in paraffin wax for microtomy and sectioned
875 at 5 μm thickness onto SuperFrost Plus charged glass slides. Sections were dewaxed and
876 rehydrated for Hematoxylin and Eosin staining by graded ethanol washes followed by incubation
877 in hematoxylin, bluing reagent, clearing agent, and eosin before dehydration and coverslipping.
878 Brightfield images were acquired with a Zeiss Axiocam 712 color camera attached to a 0.63x
879 camera mount on a Zeiss Axio Observer 7 inverted microscope stand.

880 *Immunofluorescent staining:* Rehydrated FFPE sections of extracted microfluidic chip samples
881 were stained for protein targets on neighboring sections to histology. Antigen retrieval was
882 performed using 1µg/mL proteinase K (Fisher BP1700), followed by blocking with 10% goat
883 serum and overnight staining with primary antibodies (rabbit anti-Vimentin (Novus Biologicals
884 NBP1-31327, 1:100), mouse anti-PanCK (Origene TA190321, 1:100)). On day 2, slides were
885 incubated for 2 hours at room temperature with secondary antibodies (goat anti-rabbit 555
886 (Invitrogen A21422, 1:1000), goat anti-mouse 790 (Thermo Fisher A11357, 1:1000). Slides were
887 then counterstained with NucBlue Fixed Cell ReadyProbes DAPI Reagent (Invitrogen R37606)
888 and mounted with Prolong Diamond Antifade Mountant (Invitrogen P36970). Fluorescent images
889 were acquired using a CrestOptics X-Light V3 spinning disk confocal system (Nikon Ti2) at 40X
890 magnification.

891 *Invasion depth quantification:* Invasion depth was quantified from confocal z-stacks using ImageJ
892 acquired across engineered matrix construct sections with or without osteoclasts. Maximum
893 intensity projections were generated for visualization, and normalized invasion depth was
894 computed from full z-stack measurements. For each image, PANCK+ cells were segmented using
895 threshold-based binarization following background subtraction and size filtering to exclude
896 speckle artifacts. The invasion interface was defined relative to the original matrix surface
897 boundary. For each PANCK+ object, the maximal perpendicular distance from the matrix surface
898 was calculated and normalized to total matrix thickness to account for construct-to-construct
899 variation. Image-level measurements were aggregated within biological replicates (8 image-level
900 measurements total from 5 OSCC-only matrix samples, 7 images from 4 osteoclast-containing
901 samples) prior to statistical testing.

902 **Statistical analysis**

903 All experiments were performed in triplicate unless otherwise specified. For the experiments
904 involving the comparison of two groups, statistical analysis was performed using a two-tailed,
905 unpaired Student's t-test (Prism 10 GraphPad software). For the experiments involving more than
906 two groups, one-way analysis of variance with Tukey's post-hoc test for multiple comparisons was
907 used. The statistical analysis of heatmaps for multiplex analysis by Luminex and gene comparisons
908 (NanoString) was performed using R Studio (version 2023.12.0). A p-value of 0.01 or lower for
909 gene analysis and 0.05 or lower for all the other analyses was considered statistically significant.

To assess differences in invasion depth in FFPE-sectioned matrix between conditions, we utilized a linear mixed-effects model where the condition (with or without osteoclasts) was modeled as a fixed effect, with biological replicate as a random effect to account for nested image-level measurements. A Kolmogorov-Smirnov (KS) test was used to assess distributional shifts in normalized invasion depth between conditions, and Levene's test was used to assess differences in variance between groups. Confidence intervals are reported at 95%.

Acknowledgements

We acknowledge funding from the Cancer Early Detection Advanced Research (CEDAR) Center at Oregon Health & Science University (OHSU) Knight Cancer Institute. NIH/NCI/NIDCR funding: R01DE029553, R21CA263860, K99DE033689, T90DE030859, R90DE031533, and the Friends of Doernbecher Grant Program at OHSU. We also acknowledge Lacprodan® OPN-10; Arla Foods Ingredients Group for the donation of OPN. Lastly, we acknowledge the Light Microscopy Core at OHSU for support with the image analysis.

Competing Interest

Bertassoni LE holds equity and patents associated with HuMarrow Inc., RegendoDent Inc., two companies specializing in advanced tissue engineering, and other IP associated with regeneration technologies. The other authors declared that there are no conflicts of interest.

References

1. Buttgereit, F., Palmowski, A., Bond, M., Adami, G. & Dejaco, C. Osteoporosis and fracture risk are multifactorial in patients with inflammatory rheumatic diseases. *Nat Rev Rheumatol* **20**, 417-431 (2024).

2. Fuggle, N.R. *et al.* Evidence-Based Guideline for the management of osteoporosis in men. *Nat Rev Rheumatol* **20**, 241-251 (2024).

3. Foessl, I., Dimai, H.P. & Obermayer-Pietsch, B. Long-term and sequential treatment for osteoporosis. *Nat Rev Endocrinol* **19**, 520-533 (2023).

4. Organization, W.H. Musculoskeletal conditions. https://www.who.int/news-room/fact-sheets/detail/musculoskeletal-conditions#:~:text=Other%20contributors%20to%20the%20overall,YLDs)%2C%20rheumatoid%20arthritis%20(18; 2022.

5. Fois, M.G., van Griensven, M., Giselbrecht, S., Habibovic, P., Truckenmuller, R.K. & Tahmasebi Birgani, Z.N. Mini-bones: miniaturized bone in vitro models. *Trends Biotechnol* **42**, 910-928 (2024).

6. Qin, L. *et al.* Prospects and challenges for the application of tissue engineering technologies in the treatment of bone infections. *Bone Res* **12**, 28 (2024).

7. Han, Y., You, X., Xing, W., Zhang, Z. & Zou, W. Paracrine and endocrine actions of bone-the functions of secretory proteins from osteoblasts, osteocytes, and osteoclasts. *Bone Res* **6**, 16 (2018).

8. Lutolf, M.P. *et al.* Repair of bone defects using synthetic mimetics of collagenous extracellular matrices. *Nat Biotechnol* **21**, 513-518 (2003).

9. Zhu, S., Chen, W., Masson, A. & Li, Y.P. Cell signaling and transcriptional regulation of osteoblast lineage commitment, differentiation, bone formation, and homeostasis. *Cell Discov* **10**, 71 (2024).

10. Bai, L., Zhou, D., Li, G., Liu, J., Chen, X. & Su, J. Engineering bone/cartilage organoids: strategy, progress, and application. *Bone Res* **12**, 66 (2024).

11. Song, Q. *et al.* Contribution of biomimetic collagen-ligand interaction to intrafibrillar mineralization. *Sci Adv* **5**, eaav9075 (2019).

12. Lewis, K.J. *et al.* Osteocyte calcium signals encode strain magnitude and loading frequency in vivo. *Proc Natl Acad Sci U S A* **114**, 11775-11780 (2017).

13. Mahamid, J. *et al.* Mapping amorphous calcium phosphate transformation into crystalline mineral from the cell to the bone in zebrafish fin rays. *Proc Natl Acad Sci U S A* **107**, 6316-6321 (2010).

14. Niu, L.N. *et al.* Collagen intrafibrillar mineralization as a result of the balance between osmotic equilibrium and electroneutrality. *Nat Mater* **16**, 370-378 (2017).

15. Kim, D., Lee, B., Thomopoulos, S. & Jun, Y.S. The role of confined collagen geometry in decreasing nucleation energy barriers to intrafibrillar mineralization. *Nat Commun* **9**, 962 (2018).

16. Reznikov, N., Bilton, M., Lari, L., Stevens, M.M. & Kroger, R. Fractal-like hierarchical organization of bone begins at the nanoscale. *Science* **360** (2018).

17. Gupta, H.S., Seto, J., Wagermaier, W., Zaslansky, P., Boesecke, P. & Fratzl, P. Cooperative deformation of mineral and collagen in bone at the nanoscale. *Proc Natl Acad Sci U S A* **103**, 17741-17746 (2006).

18. Rodriguez, D.E. *et al.* Multifunctional role of osteopontin in directing intrafibrillar mineralization of collagen and activation of osteoclasts. *Acta Biomater* **10**, 494-507 (2014).

19. Zhu, L., Luo, D. & Liu, Y. Effect of the nano/microscale structure of biomaterial scaffolds on bone regeneration. *Int J Oral Sci* **12**, 6 (2020).

20. Grunewald, T.A. *et al.* Mapping the 3D orientation of nanocrystals and nanostructures in human bone: Indications of novel structural features. *Sci Adv* **6**, eaba4171 (2020).

21. Wang, L., You, X., Zhang, L., Zhang, C. & Zou, W. Mechanical regulation of bone remodeling. *Bone Res* **10**, 16 (2022).

22. Thi, M.M., Suadicani, S.O., Schaffler, M.B., Weinbaum, S. & Spray, D.C. Mechanosensory responses of osteocytes to physiological forces occur along processes and not cell body and require alphaVbeta3 integrin. *Proc Natl Acad Sci U S A* **110**, 21012-21017 (2013).

23. Dupont, S. *et al.* Role of YAP/TAZ in mechanotransduction. *Nature* **474**, 179-183 (2011).

24. Wang, L., You, X., Lotinun, S., Zhang, L., Wu, N. & Zou, W. Mechanical sensing protein PIEZO1 regulates bone homeostasis via osteoblast-osteoclast crosstalk. *Nat Commun* **11**, 282 (2020).

25. Youlten, S.E. *et al.* Osteocyte transcriptome mapping identifies a molecular landscape controlling skeletal homeostasis and susceptibility to skeletal disease. *Nat Commun* **12**, 2444 (2021).

26. McHugh, J. Osteocyte death promotes bone loss. *Nat Rev Rheumatol* **16**, 539 (2020).

27. Wilson, C. Osteocytes, RANKL and bone loss. *Nat Rev Endocrinol* **7**, 693 (2011).

28. Shi, T. *et al.* Osteocyte-derived sclerostin impairs cognitive function during ageing and Alzheimer's disease progression. *Nat Metab* **6**, 531-549 (2024).

29. Owen, R. & Reilly, G.C. In vitro Models of Bone Remodelling and Associated Disorders. *Front Bioeng Biotechnol* **6**, 134 (2018).

30. Park, Y., Sato, T. & Lee, J. Functional and analytical recapitulation of osteoclast biology on demineralized bone paper. *Nat Commun* **14**, 8092 (2023).

31. Ren, X. *et al.* Osteoprotegerin reduces osteoclast resorption activity without affecting osteogenesis on nanoparticulate mineralized collagen scaffolds. *Sci Adv* **5**, eaaw4991 (2019).

32. Costa, D.O. *et al.* The differential regulation of osteoblast and osteoclast activity by surface topography of hydroxyapatite coatings. *Biomaterials* **34**, 7215-7226 (2013).

33. Duarte, J.H. Rheumatoid arthritis: Osteoclasts and ACPAs--the joint link. *Nat Rev Rheumatol* **12**, 69 (2016).

34. Ueki, Y. *et al.* Increased myeloid cell responses to M-CSF and RANKL cause bone loss and inflammation in SH3BP2 "cherubism" mice. *Cell* **128**, 71-83 (2007).

35. Kim, M.K., Paek, K., Woo, S.M. & Kim, J.A. Bone-on-a-Chip: Biomimetic Models Based on Microfluidic Technologies for Biomedical Applications. *ACS Biomater Sci Eng* **9**, 3058-3073 (2023).

36. Phillips, R. Progress toward 'bone-on-a-chip'. *Nat Rev Rheumatol* **19**, 463 (2023).

37. Wang, J.S. *et al.* Control of osteocyte dendrite formation by Sp7 and its target gene osteocrin. *Nat Commun* **12**, 6271 (2021).

38. Thrivikraman, G. *et al.* Rapid fabrication of vascularized and innervated cell-laden bone models with biomimetic intrafibrillar collagen mineralization. *Nat Commun* **10**, 3520 (2019).

39. Subbiah, R. *et al.* Engineering of an Osteoinductive and Growth Factor-Free Injectable Bone-Like Microgel for Bone Regeneration. *Adv Healthc Mater* **12**, e2200976 (2023).

40. Boskey, A. & Pleshko Camacho, N. FT-IR imaging of native and tissue-engineered bone and cartilage. *Biomaterials* **28**, 2465-2478 (2007).

41. Dallas, S.L. & Bonewald, L.F. Dynamics of the transition from osteoblast to osteocyte. *Ann N Y Acad Sci* **1192**, 437-443 (2010).

42. Qin, L., Liu, W., Cao, H. & Xiao, G. Molecular mechanosensors in osteocytes. *Bone Res* **8**, 23 (2020).

43. Diegel, C.R. *et al.* Inhibiting WNT secretion reduces high bone mass caused by Sost loss-of-function or gain-of-function mutations in Lrp5. *Bone Res* **11**, 47 (2023).

44. He, J. *et al.* Dissecting human embryonic skeletal stem cell ontogeny by single-cell transcriptomic and functional analyses. *Cell Res* **31**, 742-757 (2021).

45. Zhang, X. *et al.* Divide-and-conquer strategy with engineered ossification center organoids for rapid bone healing through developmental cell recruitment. *Nat Commun* **16**, 6200 (2025).

46. Delgado-Calle, J. & Bellido, T. The osteocyte as a signaling cell. *Physiol Rev* **102**, 379-410 (2022).

47. Xiong, J., Piemontese, M., Thostenson, J.D., Weinstein, R.S., Manolagas, S.C. & O'Brien, C.A. Osteocyte-derived RANKL is a critical mediator of the increased bone resorption caused by dietary calcium deficiency. *Bone* **66**, 146-154 (2014).

48. Wang, X., Ji, L., Wang, J. & Liu, C. Matrix stiffness regulates osteoclast fate through integrin-dependent mechanotransduction. *Bioact Mater* **27**, 138-153 (2023).

1095 49. Glantschnig, H., Fisher, J.E., Wesolowski, G., Rodan, G.A. & Reszka, A.A. M-CSF,
1096 TNFalpha and RANK ligand promote osteoclast survival by signaling through mTOR/S6
1097 kinase. *Cell Death Differ* **10**, 1165-1177 (2003).

1098
1099 50. Stegen, S. *et al.* Osteocytic oxygen sensing controls bone mass through epigenetic
1100 regulation of sclerostin. *Nat Commun* **9**, 2557 (2018).

1101
1102 51. Wei, Z. *et al.* Osteostaticytes: A novel osteoclast subset couples bone resorption and bone
1103 formation. *J Orthop Translat* **47**, 144-160 (2024).

1104
1105 52. Mun, S.H., Park, P.S.U. & Park-Min, K.H. The M-CSF receptor in osteoclasts and beyond.
1106 *Exp Mol Med* **52**, 1239-1254 (2020).

1107
1108 53. Curtis, J.R. *et al.* Comparative effectiveness of denosumab vs alendronate among
1109 postmenopausal women with osteoporosis. *J Bone Miner Res* **39**, 826-834 (2024).

1110
1111 54. Fitzpatrick, D., Lannon, R. & McCarroll, K. Postmenopausal Osteoporosis. *N Engl J Med*
1112 **390**, 675 (2024).

1113
1114 55. Fisher, J.E. *et al.* Alendronate mechanism of action: geranylgeraniol, an intermediate in the
1115 mevalonate pathway, prevents inhibition of osteoclast formation, bone resorption, and
1116 kinase activation in vitro. *Proc Natl Acad Sci U S A* **96**, 133-138 (1999).

1117
1118 56. Park, J. *et al.* CCL28-induced RARbeta expression inhibits oral squamous cell carcinoma
1119 bone invasion. *J Clin Invest* **129**, 5381-5399 (2019).

1120
1121 57. Mansoorifar, A., Gordon, R., Bergan, R. & Bertassoni, L.E. Bone-on-a-chip: microfluidic
1122 technologies and microphysiologic models of bone tissue. *Adv Funct Mater* **31** (2021).

1123
1124 58. Sun, W. *et al.* Neuro-bone tissue engineering: emerging mechanisms, potential strategies,
1125 and current challenges. *Bone Res* **11**, 65 (2023).

1126
1127 59. Staines, K.A. *et al.* Hypomorphic conditional deletion of E11/Podoplanin reveals a role in
1128 osteocyte dendrite elongation. *J Cell Physiol* **232**, 3006-3019 (2017).

1129
1130 60. Weivoda, M.M. *et al.* Identification of osteoclast-osteoblast coupling factors in humans
1131 reveals links between bone and energy metabolism. *Nat Commun* **11**, 87 (2020).

1132

1133 61. Tiskratok, W., Yamada, M., Watanabe, J., Pengyu, Q., Kimura, T. & Egusa, H.
1134 Mechanoregulation of Osteoclastogenesis-Inducing Potentials of Fibrosarcoma Cell Line
1135 by Substrate Stiffness. *Int J Mol Sci* **24** (2023).

1136
1137 62. Takegahara, N., Kim, H. & Choi, Y. Unraveling the intricacies of osteoclast differentiation
1138 and maturation: insight into novel therapeutic strategies for bone-destructive diseases. *Exp*
1139 *Mol Med* **56**, 264-272 (2024).

1140
1141 63. Kim, H.J., Kang, W.Y., Seong, S.J., Kim, S.Y., Lim, M.S. & Yoon, Y.R. Follistatin-like 1
1142 promotes osteoclast formation via RANKL-mediated NF-kappaB activation and M-CSF-
1143 induced precursor proliferation. *Cell Signal* **28**, 1137-1144 (2016).

1144
1145 64. Alshbool, F.Z. & Mohan, S. Emerging multifunctional roles of Claudin tight junction
1146 proteins in bone. *Endocrinology* **155**, 2363-2376 (2014).

1147
1148 65. Choi, S.J., Han, J.H. & Roodman, G.D. ADAM8: a novel osteoclast stimulating factor. *J*
1149 *Bone Miner Res* **16**, 814-822 (2001).

1150
1151 66. Xu, H. *et al.* Targeting strategies for bone diseases: signaling pathways and clinical studies.
1152 *Signal Transduct Target Ther* **8**, 202 (2023).

1153
1154 67. Plotkin, L.I., Weinstein, R.S., Parfitt, A.M., Roberson, P.K., Manolagas, S.C. & Bellido, T.
1155 Prevention of osteocyte and osteoblast apoptosis by bisphosphonates and calcitonin. *J Clin*
1156 *Invest* **104**, 1363-1374 (1999).

1157
1158 68. El-Masri, B.M. *et al.* Mapping RANKL- and OPG-expressing cells in bone tissue: the bone
1159 surface cells as activators of osteoclastogenesis and promoters of the denosumab rebound
1160 effect. *Bone Res* **12**, 62 (2024).

1161
1162 69. Fu, Q. *et al.* Reduced osteoprotegerin expression by osteocytes may contribute to rebound
1163 resorption after denosumab discontinuation. *JCI Insight* **8** (2023).

1164
1165 70. Jin, W. *et al.* Engineered osteoclasts as living treatment materials for heterotopic
1166 ossification therapy. *Nat Commun* **12**, 6327 (2021).

1167
1168 71. Gu, C. *et al.* Targeting initial tumour-osteoclast spatiotemporal interaction to prevent bone
1169 metastasis. *Nat Nanotechnol* **19**, 1044-1054 (2024).

1170

1171 72. Jackett, K.N., Browne, A.T., Aber, E.R., Clements, M. & Kaplan, R.N. How the bone
1172 microenvironment shapes the pre-metastatic niche and metastasis. *Nat Cancer* **5**, 1800-
1173 1814 (2024).

1174
1175 73. Gormley, M., Creaney, G., Schache, A., Ingarfield, K. & Conway, D.I. Reviewing the
1176 epidemiology of head and neck cancer: definitions, trends and risk factors. *Br Dent J* **233**,
1177 780-786 (2022).

1178
1179 74. Chow, L.Q.M. Head and Neck Cancer. *N Engl J Med* **382**, 60-72 (2020).

1180
1181 75. Elmusrati, A.A., Pilborough, A.E., Khurram, S.A. & Lambert, D.W. Cancer-associated
1182 fibroblasts promote bone invasion in oral squamous cell carcinoma. *Br J Cancer* **117**, 867-
1183 875 (2017).

1184
1185 76. Nakamura, K. *et al.* The periosteum provides a stromal defence against cancer invasion
1186 into the bone. *Nature* **634**, 474-481 (2024).

1187
1188 77. Liu, F. *et al.* Single-cell profiling of bone metastasis ecosystems from multiple cancer types
1189 reveals convergent and divergent mechanisms of bone colonization. *Cell Genom*, 100888
1190 (2025).

1191
1192 78. Mandal, M. *et al.* Epithelial to mesenchymal transition in head and neck squamous
1193 carcinoma: association of Src activation with E-cadherin down-regulation, vimentin
1194 expression, and aggressive tumor features. *Cancer* **112**, 2088-2100 (2008).

1195
1196 79. Wei, S.C. *et al.* Matrix stiffness drives epithelial-mesenchymal transition and tumour
1197 metastasis through a TWIST1-G3BP2 mechanotransduction pathway. *Nat Cell Biol* **17**,
1198 678-688 (2015).

1199
1200 80. Kfoury, Y. *et al.* Human prostate cancer bone metastases have an actionable
1201 immunosuppressive microenvironment. *Cancer Cell* **39**, 1464-1478 e1468 (2021).

1202
1203 81. Schindelin, J. *et al.* Fiji: an open-source platform for biological-image analysis. *Nat*
1204 *Methods* **9**, 676-682 (2012).

1205

1206